TECHNICAL REVIEW / SYNTHÈSE TECHNIQUE

Charge and state population in dilute plasmas from beam-foil spectroscopy

C.T. Chantler

Abstract: Beam-foil spectroscopy has a long history for determining charge state evolution, radiative decay lifetimes, spectral widths, and satellite structure. Many theoretical results predict a range of populations and state dependencies, but high resolution or a very large bandpass is normally required to test or investigate these. The current investigation has tested some key assumptions and models as applied to this relativistic regime, particularly for few-electron iron resonances and satellites. We conclude that there are two specific production mechanisms, one inside the target to low-n levels and one dominated by capture mechanisms at the exit of the foil, with particularly significant Rydberg cascades. Several systematics in high-precision measurements of these systems are discussed and quantified for the first time. The $2s$–$1s$ and $4f$–$2p$ satellites are explicitly investigated, and a dominant systematic is uncovered that is due to the variable location of spectral emission, downstream of the beam-foil target.

PACS Nos.: 32.70.Jz, 34.10.+x, 52.20.Hv, 34.60.+z

Résumé : La spectroscopie à faisceau lame est depuis longtemps utilisée pour déterminer l’évolution des états chargés, les temps de vie par désintégration radiative, les largeurs spectrales et les structures satellites. Plusieurs résultats théoriques prédisent tout un domaine de populations et de dépendances sur les états, mais cela exige une haute résolution ou une grande largeur de bande pour les tester ou les étudier. Dans cette étude nous testons certains modèles et hypothèses clés appliqués au régime relativiste, en particulier aux résonances à peu d’électrons et aux satellites dans le fer. Nous concluons qu’il y a deux mécanismes distincts de production, un à l’intérieur de la cible vers les niveaux à n petit et l’autre dominé par les mécanismes de capture à la sortie de la cible, avec des cascades de Rydberg très significatives. Nous analysons et quantifions pour la première fois plusieurs caractéristiques systématiques dans ces mesures de haute précision. Les satellites $2s$–$1s$ et $4f$–$2p$ sont étudiés explicitement et nous découvrons une dominante systématique qui est due à la localisation variable de l’émission spectrale le long du faisceau sortant de la cible.

[Traduit par la Rédaction]

1. Introduction

Beam-foil spectroscopy has developed strongly since the seminal work by Kay and Bashkin et al. in the 1960s [1–3]. Major conference series and proceedings have been devoted to the understanding of the structure observed for a wide range of fields, including astrophysics [4, 5], surface physics [6], plasma physics [7, 8], applied spectroscopy [9], and accelerator-based atomic physics [10]. Particularly exciting results have been obtained for oscillator strengths [11], transition probabilities [12], lifetimes and fluorescence yields [13], theoretical modelling [14], multi-electron spectroscopy [15], multiply-excited states and Auger electrons [16], Lamb shifts in hydrogenic and helium-like ions [17–19]. There have been numerous extensive reviews [12, 20, 21].

In the last decade, attention has turned somewhat to electron beam ion traps (EBITs) and storage rings for some particular applications, but a large range of investigations in atomic and nuclear physics has continued, especially including remarkable work on lifetime studies. One of the continuing dilemmas has been the validity of theoretical formalisms for relative population methods in the dilute plasmas of interest. While lifetimes can be measured very accurately, for example, there are particular limitations due to possible cascade processes. Of course, the significance of these varies from one particular beam to another, and often the foil or target thicknesses are such that the populations are felt to approach an equilibrium value, especially regarding charge exchange. This regime is in itself difficult to then evaluate theoretically or to impute causes, not least because of the complexity of the capture, excitation, and ionization processes in partially ionized systems.

The general problem of understanding excitation, ionization, and capture processes in plasmas is quite profound. Plasma diagnostics are crucial for tokamak design, monitoring, and development; for the interpretation of laser fusion experiments; and for aspects of nonlinear high-harmonic generation. Within accelerator and EBIT plasmas, the knowledge develops the util-

Received 6 September 2007. Accepted 7 September 2007. Published on the NRC Research Press Web site at http://cjp.nrc.ca/ on 14 March 2008.

C.T. Chantler. School of Physics, University of Melbourne, Victoria 3010, Australia (e-mail: chantler@physics.unimelb.edu.au).

doi: 10.1139/P07-173

ity of such sources for the selectivity and optimization of highly ionized charge state selection for a range of fundamental experiments.

This paper presents data taken at the Lawrence Berkeley Laboratory, Berkeley, California, on the SuperHilac linear accelerator. Results are presented for hydrogenic spectra of iron, Fe^{25+} and in particular for the Lyman and Balmer series. The target foils are kept near the single-interaction regime so that, in principle, the conditions are most amenable to theoretical comparison and are in fact quite far from equilibrium. The spectra obtained are, therefore, least affected by satellites and most insightful for a comparison of different mechanisms and models.

We use Bragg diffracting crystals for collecting photons from de-excitation processes and providing the spectral resolution necessary for precision calibrations. In particular, we use the dual-arm Johann curved crystal spectrometer SS1 designed and constructed at Lawrence Livermore National Laboratory [22, 23].

One of the key observations in different contexts for beam-foil spectroscopy is the existence of cascade transitions especially for lifetime studies. A key question asks where these decays arise (if they indeed exist).

In past beam-foil tests of quantum electrodynamics (QED) and other investigations, it has been assumed that prompt or in-target excitation and decay dominated, and any downstream shift was neglected [24]. However, some recent work has claimed that "the $2p$ states of interest in hydrogen-like Ni^{27+} are populated by one-electron capture mainly into higher n states followed by cascade transitions" [25]. This was not used in that work to compute a corresponding correction, but might imply that whatever the source mechanism, the decays would be a significant distance downstream. Lifetime studies in general assume and require that decays are prompt. Where single or perhaps double-step cascades are involved, accurate lifetimes may still be extracted from the data, depending upon the relative lifetimes of these cascades and their origin. Where the transitions become too complex for whatever reason, possibly including multiple unresolved species, the lifetime approach tends to be unsuccessful.

For an experiment to yield accurate tests of QED [26], we must develop this understanding on the firm basis of experimental data, modelling, and a theoretical underpinning. Two clear processes may be readily postulated: a C1 component of the intensities of a given Lyman or Balmer spectrum that increases with thickness, and a C2 component that does not. To first order, we might consider the latter to correspond to the "single-interaction regime" and the former to correspond to multiple excitations or ionizations within the foil. We might also expect that multiple-electron capture and the relative intensities of dielectronic satellites and related processes would increase with thickness (i.e., that they would be dominated by the C1 component), tending towards some asymptote at equilibrium.

Electron capture may occur throughout the foil or at the exit or last layer of the foil. Excitation will occur in this process, but may also occur subsequently through the foil or at the exit. Radiative decay will primarily occur downstream of the foil, but may be augmented by fields at the exit and wake fields and collisional processes inside the target.

2. Overview

This paper presents basic experimental details in Sect. 3. It discusses the technique of in-beam Lyman α–Balmer β intercomparison in Sect. 4. Photographic detection similar to the use of image plates is used as discussed in Sect. 5. Several areas crucial for accurate tests of QED are given in a companion paper [26], especially including diffraction theory systematics and corrections. A brief discussion of theoretical wavelengths for transitions is given in Sect. 6, because solid-state detectors can generally not distinguish between states or multiplets, but the current data clearly separate dominant components. A consistent interpretation depends in part on the calibration scale, which we therefore describe. Modelling of the interactions is discussed in detail in Sect. 8 beginning with the quantification of observed normalized ratios, discussion of polarization dependencies, helium-like transitions, and traditional dielectronic species, but then leading to new discussion of Lyman γ $3l$–$1s$, Lyman $2s$–$1s$, and Balmer $4f$–$2p$ contributions, a significant uncertainty in past modelling that is addressed in this work. Section 9 gives preliminary qualitative observations that do not depend upon detailed modelling, followed by a detailed discussion of theoretical models in Sect. 10. Armed with this, we tabulate model predictions compared with experimental data in Sect. 11. Section 12 discusses additional evidence from other data analysis and the companion paper [26], leading to our final conclusions in Sect. 13.

3. Experimental

A 500 $\mu\mathrm{g\,cm^{-2}}$ carbon stripper foil was used to produce an equilibrium distribution of charge states. Of this distribution, 400 nA average of bare Fe^{26+} (or about 2% of the total) is selected with a bending magnet for delivery to the target. The energies used were 8.3 MeV/amu or approximately 480 MeV, $\beta \simeq 0.1335$, with a series of exposures of from 1.3 to 11.9 mC on a carbon foil target of 5, 9, 25, 50, or 223 $\mu\mathrm{g\,cm^{-2}}$. These variations help to confirm the assumption that the thin foils corresponded to a single capture and excitation process [27]. A series of multiple collisions and electron capture – ionization processes would decelerate the beam and produce predominantly helium-like and lithium-like spectra. This satellite contamination has been a significant problem in QED experiments, but is conclusively ruled out by observed spectra.

Charge-state analysis has been conducted in relatively large detail [28, 29], so it is understood that *equilibrium* populations of $Z = 26$, $E = 8.74$ MeV/amu ($\beta = 0.1360$), $E = 8.57$ MeV/amu ($\beta = 0.1347$) are given in Table 1. With bare incident charges, competing processes are one- and two-electron capture, and the former is dominant for the thin targets used herein. As thicknesses approach equilibrium values, the effects of straggling and stopping-power become significant, multiple collisions lead to two-electron capture, and excitation and ionization processes become more important. The range for iron is approximately 18 $\mathrm{mg\,cm^{-2}}$, with stopping powers of 21(1) MeV/($\mathrm{mg\,cm^{-2}}$) [30–32]. For the best (5–10 $\mu\mathrm{g\,cm^{-2}}$) targets, this effect is insignificant, compared with the uncertainty in the incident beam velocity. Straggling broadens the profile symmetrically and contributes no shift.

Table 1. Equilibrium charge state fractions.

		Q (charge fraction %)						
Z	β	26	25	24	23	22	21	20
26	0.1360	2.5	17.1	35.8	29.8	11.9	2.6	0.4
	0.1347	2.3	16.2	35.2	30.4	12.6	2.9	0.4
	0.1326	1.9	14.6	34.1	31.5	13.9	3.4	0.5

X-rays emitted within the target may be re-absorbed by the foil. This depends on the geometry. Non-normal target angles to the beam limit the path length through the foil to the thicknesses involved. For 1.3, 1.75, and 7.0 keV radiation (Fe Balmer α, β, and Lyman α) with a thickness of 50 μg cm^{-2}, this gives 5.4%, 2.2%, and 0.03% attenuation, respectively. Thus, radiation is not significantly re-absorbed even by the thick foils and observation is limited by the foil holder and possible target distortion.

The spatial distribution of X-rays is distorted by the Doppler effect. A distribution spherical in the emission frame leads to concentration factors of 1.31 in the forward direction for $\beta = 0.1347$, but these factors are unity for our observation angle at 90° and are the same for all intensities.

Upstream energy measurements and downstream Faraday cups combined with observations of beam location and profile using TV cameras and scintillating crystals inserted into the beam. Upstream collimators of 7 mm diameter were used to control the size and alignment of the beam on the target and to allow the operators to obtain a more ideal low-divergence focus at the target. Reference anode sources of Ni.S.Si mixtures were used in situ to confirm the spectrometer alignment, but these are low-precision references compared with the in-beam calibration lines (because of their nonideal anode composition profile and the large relative Doppler shifts involved).

Two sealed proportional counters view the foil through slits aligned with the dispersion plane of the spectrometer, allowing the foil to be positioned [26]. A dispersion plane must be defined and should be identical for both arms of the spectrometer. All components are symmetrically located with respect to this plane, and crystals and film planes must lie on their respective Rowland circles satisfying the Johann geometry. The Rowland circle radius is $R = 150$ mm, while the distance from the foil centre to the crystals is approximately 26 mm. Crystals are selected for maximum illumination in the middle of the Bragg angle range and for favourable Balmer and Lyman reflectivities.

4. Lyman α – Balmer β alignment and spectrometry

In-beam calibration is not normally possible because of the absence of hydrogenic or helium-like spectral lines near the Lyman α region with limited-range or scanning spectrometers and with the use of first-order diffraction of the Lyman α radiation. However, Lyman α radiation is nearly exactly four times the energy of Balmer β radiation, with deviations following from relativistic and QED corrections to the Bohr model. Thus, diffraction of Lyman α radiation in fourth order with appropriate crystals will provide an in-beam calibration source with the same ions (and ion velocities), so that the Doppler-shift is identical for all lines. This then provides a precise $n = 2$–1 versus $n = 4$–2 Lamb shift measurement [33]. This comparison involves a quite different principle from the use of multiple references to many-electron in-beam calibration lines [34].

The strong $2p$–$4d$ components lie on either side of the $1s$–$2p$ transitions, and crystal resolution in the $Z = 22$–40 region is adequate to fully resolve the $2p_{3/2}$–$1s$ and $2p_{1/2}$–$1s$ Lyman $\alpha_{1,2}$ transitions. Diffracting efficiencies for both first- and fourth-order lines yield good statistics in a reasonable period of accelerator beam time. The vacuum chamber supporting the spectrometer has vertical and horizontal adjustments, allowing the spectrometer to be positioned normal to the beam-line with a transit, with the foil location and spectrometer base-plate centred on this axis. The height of all components (slits, magnetic baffles, spectrometer baffles, film holders, and crystals) is set with a depth micrometer so that the observation plane is 1.1 in (1 in = 2.54 cm) above the base-plate. All spectrometer components are equipped with kinematic mounts. Detectors and crystal mounts are positioned on the Rowland circle using a rotating jig equipped with a dial gauge. This rotates around a defined Rowland circle centre to position the film holders (and estimate the crystal surface at its centre, where it should meet the Rowland circle). Kinematic mounts are reproducible to 0.025 mm, while detector planes are accurate to 0.05 mm around the circle.

Magnetic baffles with a 60 mm × 4.5 mm aperture are used to deflect scattered charged particles (particularly electrons). The spectrometer baffles have five horizontal wires that test the overall alignment of source, crystal, and baffles. The film window covers Bragg angles from 27.6° to 72°, reduced by the spectrometer baffle and crystal range to approximately 35°–53° for uniform source intensity (the whole source being imaged by the crystal) or 28°–58° (roughly half of the source imaged by the crystal). Target frames are 20.6 mm × 20.6 mm × 0.5 mm, with an internal circular diameter of 19 mm. They are mounted in a collimating target holder with the (carbon) foil downstream to avoid occlusion of X-rays from the rear surface.

5. Photographic detection

A deviation from conventional Lamb-shift measurement relates to the use of photographic detection and the finite source location lying well inside the Rowland circle. This simultaneously observes the whole spectrum, focused, eliminating errors from beam fluctuations in energy, location, angle, and intensity (to first and second order) and reducing collection times per experiment.

X-rays are detected with Kodak DEF-392 X-ray film, mounted in aluminium holders to lie along the Rowland circle. The light-tight holders have a removable rear for mounting and removing the film, which is fixed against the inside front surface by the rear during exposures. X-rays enter through aluminium-coated Mylar windows. Efficiency is limited by window absorption and transmission factors, compensated for by the increased reflectivity of the curved crystal spectrometer. Photographic detection also yields the highest resolution detection system available, limited by cluster sizes of 2–3 μm.

Film is developed in a Patterson tank for 5 min in Kodak D-19 at 68 °F (20 °C), agitating every 30 s, followed by 30 s in a stop bath, and 9 min in Kodak rapid fixer (with regular agitation). The film is then washed and left to dry. Developer was made up for calibration exposures and at regular intervals, and exposure to the air was minimized.

Densitometry is a fascinating area where new theory has been necessary to interpret the experimental data to the precision required. This is discussed elsewhere [35–38]. Theoretical difficulties relate to the determination of absolute and relative intensities from the raw specular density data and in the alignment parameters and variables of the densitometry process itself. These issues should not distort derived spectral centroids if addressed. Linearised relative intensities are derived with absolute accuracy given by the pseudo-binomial grain statistic, so that spectra of $(I \pm \delta I)$ along two dimensions may then be used as inputs for later analysis. An important change to previous work involved the automated and simultaneous densitometry of whole films, preserving the two-dimensional orientation, and the densitometer angular and positional variables. The software used to analyse the data and propagate the error field using least-squares minimization (including Levenberg–Marquardt, singular value decomposition, and Monte-Carlo techniques) was developed for this purpose [38].

6. Theoretical input, Doppler shifts, and analytic development

For $n = 1$ and 2 levels, the source of theoretical wavelengths for comparison with experiment is straightforward, given the agreement between results for the two most comprehensive computations [39, 40]. However, this is not true for the higher n levels and hence the Balmer transition energies. Values of Erickson [41] must be corrected for improved values of constants, Dirac energies, and QED terms [38], particularly the Bethe-logarithms [42]. Estimated theoretical uncertainties in the resulting wavelengths lie at the few parts per million (ppm) level. Helium-like resonance transitions can be observed, and values for these states follow Drake [43] and Vainshtein [44], with corrections of the latter following Drake for higher n levels [38]. Because of these corrections, a detailed summary of relevant theoretical transition energies is given in ref. 26, but energies are depicted for dominant transitions in Figs. 1 and 2.

The strongest Balmer line (Balmer β_1, $2p_{3/2}$–$4d_{5/2}$) was used as the reference line. Fits of individual spectral regions allow the consistent use of background levels and widths of the two Lyman α peaks and the seven Balmer β components. Common widths were assumed for each Balmer component, and similarly for the two Lyman components. Lorentzian profiles convolved with aperture functions or Voigt profiles were generally required (neither Gaussian nor Lorentzian profiles adequately represent the peak profiles).

7. Fitted relative component intensities

The scale of the Balmer spectra can be used to measure and constrain any centroiding error. Relative intensity variation can confirm any such correlated error or uncertainty.

Fig. 1. Summary of the dominant Lyman series transitions diffracted in third or fourth order in this experiment. All transitions are electric dipole-allowed direct transitions to the ground state. Details of energies used are presented elsewhere [26].

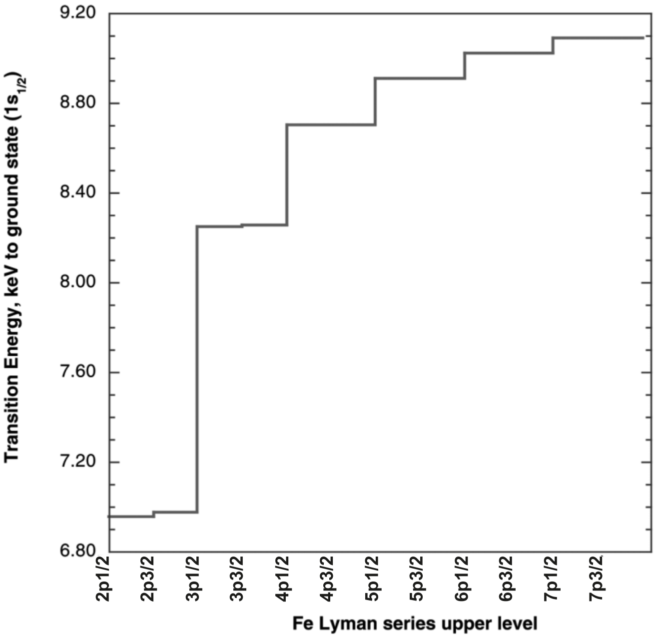

The quality of the data is indicated by Fig. 3. For low exposures and thin foils, the residuals after fits are randomly distributed, indicative of an adequate profile shape. The local χ_r^2 for an individual scan was typically 5–10 for a strong exposure as represented by the Lyman α – Balmer β region of the plot. This scaling of expected error bars is dominated by the effect of background noise and nonlinear effects in the densitometric linearization [35–37]. Specifically, the densitometry linearization relation for energies diffracting in first order is quite different from that for energies diffracting in fourth order, particularly for strong exposures where the density range is large. Centroids are well-determined, but a single linearization scheme for first-order diffraction (Balmer energies) will tend to distort peak profiles from the "other" order of diffraction. The quality of the centroid determination is thus relatively independent of the final local χ_r^2 for a single scan and well-determined by the derived centroid uncertainty. Although the film resolution is very good, the scattered electrons from the beam and the film exposure itself provides a "noisy" background exceeding counting uncertainties. Therefore, uncertainties are reported as $\sigma\sqrt{\chi_r^2}$, where σ is the output (fitted) one standard deviation uncertainty.

8. Beam-foil excitation, multi-electron transitions, and the C1 and C2 components of spectral lines

The following statement discusses understanding in the absence of detailed information relating precisely to the given experimental conditions:

Fig. 2. Summary of the dominant Balmer series transitions diffracted in first order in this experiment, covering a wide range of energies. Dominant transitions are electric dipole-allowed (E1), relativistically-allowed M1, or E2 transitions. Energies observed are discussed elsewhere [26].

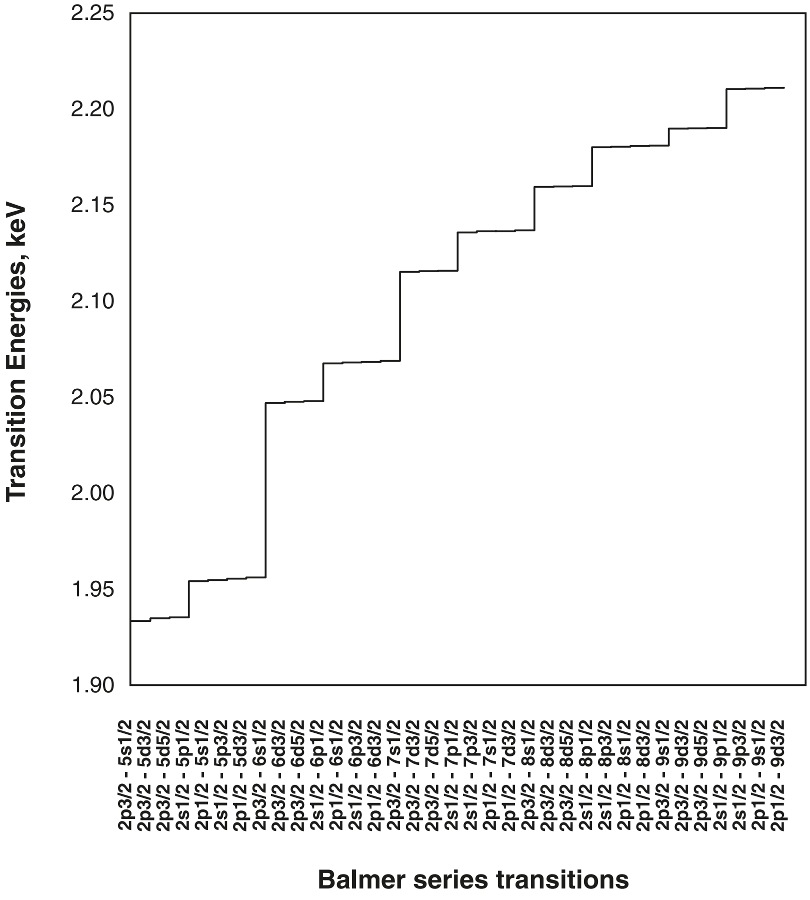

Fig. 3. An individual scan (number 10 of 18) of a particular Rowland circle (A1), emulsion (20), and densitisation (0.45 mm height) using a PET diffracting crystal for a 9 μg cm^{-2} carbon target thickness, in the region from the Balmer γ location through the the Lyman α and Balmer β region of overlap between the first and fourth orders of diffraction. From left to right, in the Balmer β region, Balmer β $2p1/2$–$4d3/2$, $2s1/2$–$4p3/2$; Balmer β $2p1/2$–$4s1/2$, $2s1/2$–$4p1/2$; Lyman α $1s1/2$–$2p3/2$; Lyman α $1s1/2$–$2p1/2$; Balmer β $2p3/2$–$4d5/2$, $2p3/2$–$4d3/2$; Balmer β $2p3/2$–$4s1/2$. Residuals are dominated by noise, indicating a consistent fit. This thin foil regime shows minimal heliumlike contamination.

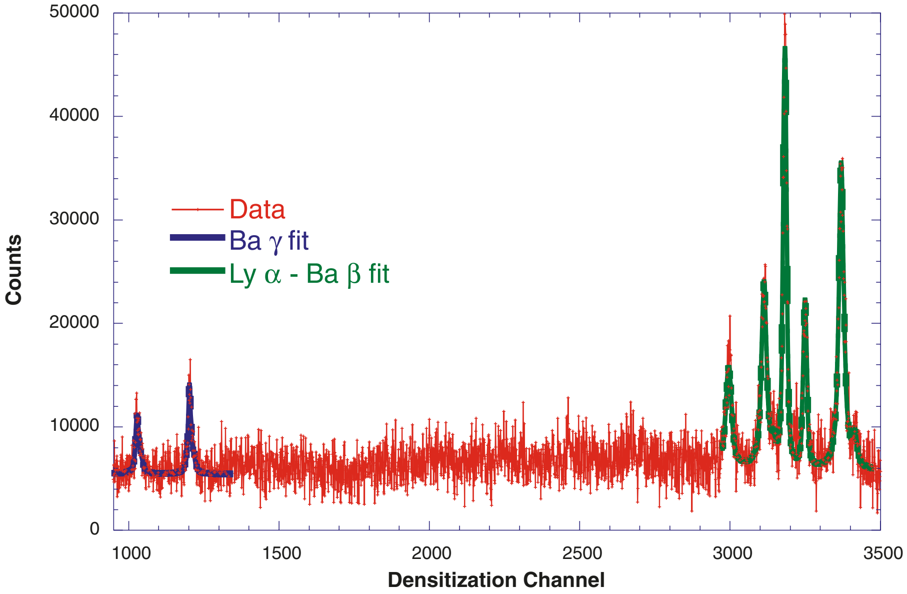

> We at best have an understanding of only some isolated aspects of the beam-foil collision process. We cannot begin to predict the population of specific atomic levels, since we have no comprehensive picture of the collision process. Ref. 45

While each experiment in the literature has provided some significant insight into these processes, the experimental data have usually been focussed on a particular species, often at low resolution, rather than an attempt to collect a picture of a population mechanism. Equally, different theoretical models vary sufficiently widely that most competing assumptions from the introduction are valid in one of the available models. Recent work and reviews have emphasized the continuing value of this type of inquiry [12, 20].

Data on intensities collected in the Lamb-shift experiments are able to differentiate between some of these alternatives. Together with the observed variation of specific components of high-n, l transition profiles in the photographic data, this proves a dependence of intensities of members of the Lyman and Balmer series spectra upon the target foil thickness.

Lyman α radiation increases by factors of 1.8 and 3.3 as the target thickness increases from 10 to 50 to 238 $\mu\mathrm{g\,cm}^{-2}$. Conversely, Balmer β, γ, and δ radiation show no increase in intensity with thickness. Balmer α and Lyman β increase by factors of 1.22 and 1.34 for $10 \rightarrow 50\,\mu\mathrm{g\,cm}^{-2}$ and 1.43 and 2.72 for $10 \rightarrow 238\,\mu\mathrm{g\,cm}^{-2}$, respectively. The transitions $1s2p$–$1s^2$ and $1s3p$–$1s^2$ increase by factors of 1.50 and 1.06 for $10 \rightarrow 50\ \mu\mathrm{g\,cm}^{-2}$ and 8.42 and 6.11 for $10 \rightarrow 238\ \mu\mathrm{g,m}^{-2}$; note uncertainties of 40%–90% for weak helium-like peaks using the thin foils.

The spectra are very far from equilibrium, with (hydrogenic: helium-like) Lyman α:$1s2p$–$1s^2$ ratios of 19.4:1.0(±0.6) for 10 $\mu\mathrm{g\,cm}^{-2}$ targets instead of the value of 0.69:1.0 expected from equilibrium charge fractions. The population of hydrogenic (and helium-like) ions might be expected to increase linearly with target thickness (or as $1 - \exp(-At)$ nearer equilibrium). This is roughly observed for helium-like states and should be true for any transition.

This summary of experimental data demonstrates that (from the lack of thickness dependence of the corresponding transitions) s, p, and d states for $n > 3$ are not populated within the foil. Therefore, excitation at the exit (the C2 component) is dominant for higher n states and gives a large contribution for all excited states, which may involve electron capture of bare ions.

Application of this conclusion suggests that 10 $\mu\mathrm{g\,cm}^{-2}$ foils have only 23%, 13%, and 2.2% radiation from this second C2 process for Lyman α, Lyman β, and Balmer α, respectively (± 2%–3%). Results obtained using ammonium dihydrogen phosphate (ADP) diffraction show differences from pentaerythritol (PET) diffraction due to the greater relative intensities of fourth-order transitions, the thinner 5 $\mu\mathrm{g\,cm}^{-2}$ target and a minor 10° target tilt angle. There has been discussions of surface structure and tilt angle in the literature relating to both channelling and relativistic cross sections; we find that the data are fully consistent for targets with different roughness, presumably orientation and minor tilt angle changes, and we do not need to invoke these issues. Of course we did not set up a channelling experiment. Agreement of Lyman ratios from ADP results with PET results after known corrections for diffraction efficiencies and exposure times is perhaps remarkable and differences are generally within experimental scatter.

Consistency of results for these thin-target exposures suggests that the intensity ratios may be used to understand the beam-foil process more deeply and perhaps explain systematic effects. Most thicker target exposures with PET were short, leading to significant noise but still sufficient accuracy.

These experimental data are summarized in Table 2 in the first three columns, indicating the relative intensities of the spectral features normalized to the strongest component of Balmer β and indicating the corresponding thickness dependence. Table 2 presents imputted thickness components for the 9 $\mu\mathrm{g\,cm}^{-2}$ target on the basis of a linear comparison with thicker targets and with an extrapolation to zero thickness. The data confirm the validity of this extrapolation. These experimental data will then be used to investigate processes that could yield these observed intensities and a series of potential effects of such processes upon apparent measured wavelength.

The Balmer β_5 $2p$–$4d$ component appears to remain the same as the target thickness is increased. Other Balmer β components also remain approximately constant; $2s$–$4p_{3/2}$ may increase by (19 ± 11)%, while the $2p_{1/2}$–$4d_{3/2}$ decreases by (8 ± 3.4)%. Such variations are likely due to fitting uncertainties.

The total $I(Ba\gamma)/I(Ba\beta_5)$ ratio is consistent with a mean of 0.513 ± 0.023, with a slope of less than $\pm 0.001/(\mu\mathrm{g\,cm}^{-2})$, including all PET and ADP results and consistent with the first iron experiment [33]. $I(Ba\delta)/I(Ba\beta_5)$ appears constant, and results for Balmer ϵ are *also* consistent with no thickness dependence.

Fourth-order PET diffraction of Lyman α suggests that 77% of the radiation for A120/B220 films is independent of thickness (C2). Compared with this, the first iron measurement [33] gives a ratio high by a factor of three. This discrepancy is likely due to different observation regions in the two experiments and to crystal diffraction effects. "A circle" values for Lyman β also imply that 76% of Lyman β radiation in A120 is independent of thickness (C2).

Helium-like $1s2p$–$1s^2$ radiation, by contrast, is 86%–100% proportional to the target thickness. The lower estimate is possible *if* a double-capture cross section is significant and the remainder increases quadratically (as the probability of two consecutive single-capture processes). Trends for other helium-like and lithium-like lines may be assumed to follow similar germanium data [38, 46] and be approximately proportional to target thickness. Satellites to Lyman and Balmer series will therefore be minimized with the thinnest targets (and with the $1 - e$ pickup experimental technique).

8.1. Polarization of spectral lines

Diffraction efficiency computations often assume pure π polarized radiation (with respect to the diffracting crystal). Unpolarized radiation would generally double any and all affected intensities, because σ polarization has negligible reflectivity. For Bragg angles far from $\pi/4$, radiation in the third-order diffraction region would increase by a smaller amount. For PET diffraction, Lyman α and Balmer β have similar intensity

Table 2. Hydrogenic iron intensities relative to Balmer β_5: experiment versus modelling, 9 μg cm^{-2} target, $\beta \simeq 0.1335$. Note that models M0, M1, and M2 are strongly "disproven" by the experimental data of C1 and C2, but these are listed to investigate regions of potential validity of these constructions and isolate observable dependencies.

	Experimental		Model predictions						
Line	C1	C2	M0	M1	M2	M3	M4	M5	M6
Ly limit	0[a]	<1.62[b]	0.19(2)	4×10^{-17}	1.02	0.64(2)	0.69(2)	0.28(2)	0.22(2)
Ly δ[b]	0	0.20(14)[c]	0.5572	2×10^{-8}	0.7291	0.2579	0.7047	0.3985	0.2844
Ba 7_{5-7}	0	0.026(13)	0.0013	1×10^{-41}	0.0790	0.0384	0.0324	0.0160	0.0120
Ba ζ_{1-4}	0	0.019(4)	0.0042	1×10^{-29}	0.1054	0.0481	0.0505	0.0201	0.0151
Ly γ[b]	0	0.91(34)	3.376	0.9170	1.554	0.6553	1.850	1.290	0.9290
Ba ζ_{5-7}	0	0.033(9)	0.0036	3×10^{-30}	0.1154	0.0721	0.0542	0.0296	0.0226
Ba ϵ_{1-4}	0	0.036(15)	0.0109	2×10^{-19}	0.1620	0.0984	0.0903	0.0403	0.0308
Ba ϵ_{5-7}	0	0.043(16)	0.0106	4×10^{-20}	0.1781	0.1487	0.0981	0.0596	0.0465
Ba δ_1	0	0.0421(53)	0.0188	4×10^{-10}	0.2052	0.1588	0.1070	0.0604	0.0497
Ba δ_2	0	0.0122(20)	0.0125	3×10^{-20}	0.0298	0.0341	0.0243	0.0150	0.0107
Ba δ_3	0	0.0088(11)	0.0005	9×10^{-28}	0.0043	0.0182	0.0248	0.0080	0.0057
Ba δ_4	0	0.0070(9)	0.0063	6×10^{-18}	0.0286	0.0171	0.0231	0.0075	0.0053
Ly β_1[b]	0.42(6)	1.32(22)	23.29	2.974	2.280	1.643	3.535	4.020	2.981
Ly β_2[b]	0.18(2)	0.58(6)	11.62	1.491	2.025	0.8265	3.193	2.018	1.497
Ba δ_5	0	0.0777(97)	0.0328	8×10^{-11}	0.2487	0.2837	0.1299	0.1079	0.0888
Ba δ_6	0	0.0100(13)	0.0036	7×10^{-11}	0.0398	0.0308	0.0208	0.0117	0.0096
Ba δ_7	0	0.0182(23)	0.0010	2×10^{-27}	0.0083	0.0352	0.0480	0.0156	0.0110
Ba γ_1	0	0.137(10)	0.0859	0.1368	0.3765	0.1620	0.2538	0.1610	0.1416
Ba γ_2	0	0.0376(25)	0.0541	1×10^{-10}	0.0546	0.0250	0.0528	0.0386	0.0276
Ba γ_3	0	0.0177(42)	0.0023	5×10^{-18}	0.0092	0.0116	0.0597	0.0232	0.0164
Ba γ_4	0	0.0190(12)	0.0270	2×10^{-9}	0.0515	0.0125	0.0496	0.0193	0.0138
Ba γ_5	0	0.241(14)	0.1497	0.2444	0.4601	0.2894	0.3112	0.2878	0.2531
Ba γ_6	0	0.0274(21)	0.0166	0.0265	0.0729	0.0314	0.0491	0.0312	0.0274
Ba γ_7	0	0.0353(85)	0.0045	9×10^{-18}	0.0178	0.0224	0.1155	0.0450	0.0318
$4f_{5/2}$–$2p_{1/2}$	—	—	0.0014	0.0049	0.0010	0.0079	0.0047	3×10^{-6}	0.0048
Ba β_1	0	0.583(12)	0.5754	0.5592	0.8076	0.5594	0.7997	0.5590	0.5592
Ba β_2	0	0.102(7)	0.3236	0.0879	0.1162	0.0627	0.1381	0.1236	0.0890
Ba β_3	0	0.0405(69)	0.0143	5×10^{-9}	0.0258	0.0365	0.1897	0.0922	0.0652
Ba β_4	0	0.0378(62)	0.1611	0.0438	0.1069	0.0314	0.1275	0.0617	0.0445
Ly α_1[b]	1.784	6.09(60)	665.4	34.18	11.18	17.50	27.99	39.81	34.09
Ly α_2[b]	0.826	2.83(28)	329.7	17.17	9.270	8.841	23.84	19.96	17.12
2s-1s	—	—	0.0032	1.508	0.2294	0.4073	2.082	1.993	1.413
$4f_{7/2}$–$2p_{3/2}$	—	—	0.0033	0.0114	0.0018	0.0183	0.0087	8×10^{-6}	0.0112
$4f_{5/2}$–$2p_{3/2}$	—	—	0.0004	0.0014	0.0003	0.0023	0.0013	1×10^{-6}	0.0014
Ba β_5	0	1.00(3)[d]	1.0	1.0	1.0	1.0	1.0	1.0	1.0
Ba β_6	0	0.1148(45)	0.1109	0.1078	0.1557	0.1079	0.1542	0.1078	0.1078
Ba β_7	0	0.075(10)	0.0276	1×10^{-8}	0.0498	0.0703	0.3658	0.1777	0.1257
Ba α	.14(20)	6.3(22)?	27.60	15.67	6.374	14.70	15.78	12.28	15.17

Note. C1: thickness-dependent components (experimental); C2: thickness-independent components (experimental); M0: result of statistical population, free decay, neglecting cascades; M1–M6: models in text including cascades ($l = n-1 \rightarrow n-3$, OBK, n^{-2} and n^{-3}, $m_l = 0$, $l = 0-2$, and statistical).

[a] Si(Li) detector results.

[b] Lyman intensities scaled by 2× for polarization correction.

[c] Fifth-order lithium-like estimate subtracted (large uncertainty).

[d] Reference line for normalization.

shifts relative to third-order lines, and the largest corresponding effects would increase this radiation by 16% and 12% compared with Balmer β and Lyman α radiation, respectively. ADP diffraction would give largest shifts for third-order lines, reducing their intensities by 24% compared with the Lyman α – Balmer β region.

These intensity shifts are *not* observed, either between the crystals or as trends with the series. Limits are placed on σ polarized radiation by the ADP crystals, the excitation cross section per beam atom, and by the consequent divergence between ADP and PET results. Specific transitions may vary in their polarization state. This would scale their relative intensities up (or down, if Balmer β is unpolarised), depending upon the observation angle.

Comparison of germanium Lyman intensities to Si(Li) detector results [38, 46, 49] suggests that photographic detection observes roughly half of the Lyman radiation (relative to Balmer intensities). A detailed analysis [36, 38, 47] concluded that iron Balmer β (i.e., nd–$2p$) radiation was significantly π polarized; Lyman radiation therefore appears to be unpolarized. This is supported by observations in the literature [48] and by a range of models.

Results for A322, B422, A317, and B417 (the fitted ADP results) all used a target tilted at 10°, which could introduce additional polarization effects and increase the effective thickness. The consistency for Balmer β, γ, Lyman β and the helium-like resonance implies that this has no significant effect upon polarization. Possible discrepancies from the consistency for C1/C2 components and polarization are marginally observed for A317 and B417 Lyman α intensities (but not for A322 and B422) and for very weak Balmer δ and $1s4p$–$1s2s$ (within a factor of 2–3, probably consistent with uncertainties) (Table 2).

8.2. Helium-like and lithium-like transitions

Relative to the iron Lyman α_1 intensity for the 5 to 9 $\mu\mathrm{g\,cm}^{-2}$ targets, fourth order $1s2p\,^1\mathrm{P}_1,^3\mathrm{P}_1$–$1s^2$, $1s3p\,^1\mathrm{P}_1,^3\mathrm{P}_2,^3\mathrm{P}_1$–$1s^2$, and $1s4p\,^1\mathrm{P}_1$+$^3\mathrm{P}_1$–$1s^2$ transitions appear to have intensity ratios of 7.5 ± 0.5%, 6.7 ± 0.8%, 2.45 ± 0.15%, 1.24 ± 0.29%, 2.38 ± 0.33%, and 4.17 ± 0.24%. Lithium-like transitions are weaker by a factor of 0.30 ± 0.02. Dominant first-order lines, relative to Balmer β_5, have been measured for $1s4p\,^3\mathrm{P}_{2,0}$–$1s2s\,^3\mathrm{S}_1$ and $1s5p\,^3\mathrm{P}_{2,0}$–$1s2s\,^3\mathrm{S}_1$, and similar transitions, to be 7.8 ± 1.5% and 2.6 ± 0.8%. For the first iron experiment, the 25 $\mu\mathrm{g\,cm}^{-2}$ target and experimental conditions increase Lyman α radiation by a factor of 3.73 relative to Balmer radiation. The ratio of $1s2p\,^1\mathrm{P}_1,^3\mathrm{P}_1$–$1s^2$ to Lyman α_1 increases by 1.64 and 1.43, and higher level radiation appears to remain roughly constant relative to this increase. Lithium-like lines may increase by 5%–30% relative to this. Contamination in that experiment was therefore more significant. Germanium results for the 10 $\mu\mathrm{g\,cm}^{-2}$ targets give ratios for $1s2p(^1\mathrm{P}_1$+$^3\mathrm{P}_1)$–$1s^2$ and $1s3p(^1\mathrm{P}_1$+$^3\mathrm{P}_1)$–$1s^2$ intensities relative to Lyman α of 5.1 ± 2.3% and 1.1 ± 0.4%.

8.3. Electric dipole and traditional dielectronic transitions

Doubly excited satellites may be expected to be at least an order of magnitude weaker than the above. This is supported by estimates based on thick 238 $\mu\mathrm{g\,cm}^{-2}$ targets [46]. Dominant contamination of Lyman α may arise from lower or higher wavelength transitions, the former arising from addition of a $2p$ spectator and the latter arising from $2s$ and $2p$ spectators [49]. All such states are unstable and have large autoionization rates, so will yield prompt and weak emission at the foil exit. There are many longer wavelength satellites and few shorter wavelength satellites.

However, the nearest $n = 2$ satellites to Lyman α_1 are $2p^2\,^1\mathrm{S}_1$–$1s2p\,^3\mathrm{P}_1$ ($\lambda = 1.7741$ Å) and $2s2p\,^1\mathrm{P}_1$–$1s2s\,^3\mathrm{S}_1$ ($\lambda = 1.7784$ Å). Quoted wavelengths are uncertain at the 0.04% level, but satellite separations will be more precise. These are resolved from the former ($\lambda/\Delta\lambda = 5\,561\,616$) so should reveal peak asymmetry if significant. Closest $n = 3$ satellites are $2s3d\,^1F_3$–$1s3d\,^1\mathrm{D}_2$ ($\lambda = 1.7765$ Å, $\lambda/\Delta\lambda = 2222$) and $2p3p\,^1\mathrm{D}_2$–$1s3p\,^3\mathrm{P}_2$ ($\lambda = 1.7776$ Å, $\lambda/\Delta\lambda = 5925$), and may give shifts only at the 1 ppm level [50]. We mention predicted shifts here because of the significance for the companion paper [26] and because any large potential shifts can be excluded by the experimental data to thereby refine the population models.

Satellites to Lyman α_2 are more numerous and closer, and involve $n = 2$ spectators. They should be three times the population of $n = 3$ spectator levels from consideration of the $1s2l$ versus $1s3l$ level populations to which they decay. The closest levels with lower autoionization rates are $2p^2\,^1\mathrm{S}_1$–$1s2p\,^1\mathrm{P}_1$ ($\lambda = 1.7823$ Å, $\lambda/\Delta\lambda = 8913$ or 1620) and $2s2p\,^1\mathrm{P}_1$–$1s2s\,^1\mathrm{S}_0$ ($\lambda = 1.7865$ Å, $\lambda/\Delta\lambda = 446$ or 575), with the first estimate assuming that satellite shifts compared with Lyman transitions are accurate and the second assuming that quoted wavelengths are accurate. Both estimates are possible within quoted Lyman α wavelength uncertainties. The $2p^2\,^1\mathrm{S}_1$–$1s2p\,^1\mathrm{P}_1$ satellite may dominate and contribute a (2–5) ppm lowering of Lyman α_2 wavelengths. These shifts should be linear with target thickness, so that 25, 50, and 238 $\mu\mathrm{g\,cm}^{-2}$ targets may have 6–13, 12–28, and 52–132 ppm effects, respectively.

The closest fourth-order satellite to Balmer β_1 transitions is $2p3p\,^1\mathrm{S}_0$–$1s3p\,^1\mathrm{P}_1$ ($\lambda = 1.7760$ Å) and is well separated. Satellites to Balmer β_5 (shifted to 1.7935 Åfor fourth-order radiation) are $2s2p\,^3\mathrm{P}_0$–$1s2s\,^3\mathrm{S}_1$ ($\lambda = 1.7926$ Å) and $2p^2\,^3\mathrm{P}_1$–$1s2p\,^3\mathrm{P}_2$ ($\lambda = 1.7935$ Å). These could shift the peak down by only 4 ppm for PET diffraction, but by 90–100 ppm for ADP diffraction!

However, energy determinations using these two disparate crystals agree, implying that these $2s2p$ transitions are weaker than this estimate by a factor of 10, with $2p^2$ weaker by a factor of two (at least). The strongest $2p^2$ transitions should be $2p^2\,^1\mathrm{D}_2$–$1s2p\,^1\mathrm{P}_1$ ($\lambda = 1.7913$ Å) or $2p^2\,^3\mathrm{P}_2$–$1s2p\,^3\mathrm{P}_2$ ($\lambda = 1.7919$ Å) under dielectronic recombination or most capture–excitation models (see Fig. 4). These transitions lie in the flat background region below Balmer β_5. Limits are provided at the 3% level for A115C and at the 1% level for B422S, where a weak peak in this region is observed in some scans. This implies that these stronger transitions lie at the 0.6 ± 0.3% level for 9 $\mu\mathrm{g\,cm}^{-2}$ targets (as quoted above), but that corresponding *satellite* transitions (above) are weaker by a factor of 5–10.

There may also be first-order satellites to Balmer β transitions from the $2p4d$, $2s4d$, and $3l4d$ states. In addition to large autoionization rates, these states will normally decay from the inner excited shell first, further reducing cross sections. Shifts are likely to be to longer wavelengths on average, but are insignificant at the 0.1 ppm level.

Revision of satellite shift estimates for 9 $\mu\mathrm{g\,cm}^{-2}$ targets in the iron experiment are then ±1 ppm, -2 ± 1 ppm, and $+0.1 \pm 0.1$ ppm for Lyman $\alpha_{1,2}$ and Balmer β_1, and -0.2 ± 0.3 ppm, -7 ± 2 ppm for PET and ADP diffraction of Balmer β_5 radiation.

8.4. Lyman γ transitions in fifth order

Lyman γ in fifth order is also diffracted to the Lyman α region, lying between the two components. Refractive index shifts are nearly identical for the two orders, so their locations in iron spectra are 0.574 and 0.674 times the Lyman α separation. The weaker $4p_{1/2}$–$1s$ component is well resolved from

Fig. 4. An individual scan (number 9 of 21) of a particular Rowland circle (B1), emulsion (1), and densitisation (0.45 mm height) using a PET diffracting crystal for a 25 μg cm^{-2} carbon target thickness, in the region from the Balmer γ location through the the Lyman α and Balmer β region of overlap between the first and fourth orders of diffraction. Scales are relative. This thicker target shows clear development of heliumlike satellites, in this region dominated by $1s5p^3P_2$–$1s2s^3S_1$, $1s5p^1P_1$–$1s2s^1S_0$, $1s5d^3D_3$–$1s2p^3P_2$, and $1s5d^1D_2$–$1s2p^1P_1$ as fitted from left to right. Error bars are underestimated by about a factor of three because of the densitometry being dominated by the nonlinear detector response.

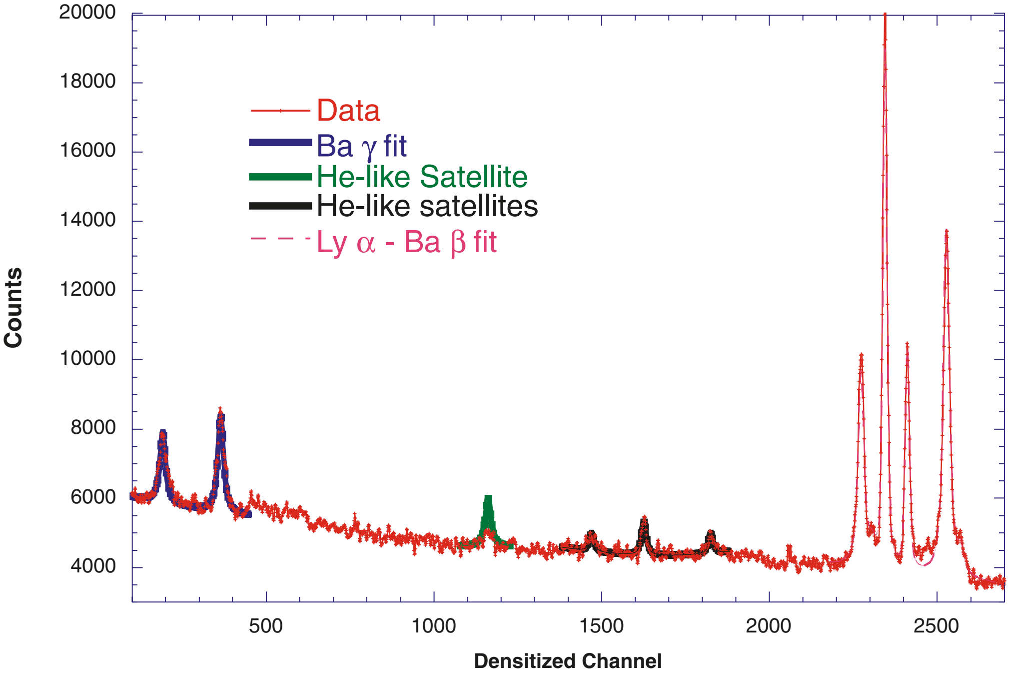

Lyman α_2 ($\lambda/\Delta\lambda < 1008$, for Fe). Expected intensities may be estimated from fourth-order Lyman γ intensities, scaled by relative diffraction efficiencies to give $I(5Ly\gamma_2)/I(4Ly\alpha_2) \simeq 1.7 \pm 0.5\%$ and $0.38 \pm 0.10\%$ for PET and ADP diffraction, respectively, in good agreement with observation of these peaks in the germanium data[1] and observation of background fitting in the best iron data. Since peaks are well resolved, this might give a shift roughly as the square of the contamination (i.e., not linearly) and may lower Lyman α_2 wavelengths by 0.29 ± 0.17 ppm for PET diffraction or negligible values for other crystals and for Lyman α_1.

Similar near-overlap occurs in other regions, notably lithium-like $1s2l2p$–$1s^22l$ in third order with Balmer η and third-order $1s2p^3P_2$–$1s^2$ with fourth-order Lyman δ. These do not affect derived relative intensity estimates since third-order lines may be measured separately in fourth-order diffraction.

8.5. 2*s*–1*s* transitions

Two-photon $2s$–$1s$ radiation will be diffracted in second order in the Lyman α region, as will the relativistic M1 component in fourth order. These are discussed in ref. 51. The two-photon fwhm is $\lambda/2$ and the lifetime would be $4.024E\times10^{-10}$ s ($Z = 26$), 1.171×10^{-10}s ($Z = 32$), or 10^5 times Lyman α, so only contributes a very weak background to the whole spectrum, most of which is emitted downstream and outside the detection region. We discuss both atomic numbers because the consistent analysis of iron and germanium data is important in relation to satellite intensities and population dynamics.

For these two elements, the rM1 component gives a lifetime of 2.838×10^{-9} s ($Z = 26$) and 3.558×10^{-10} s ($Z = 32$). For the rM1 12% ($Z = 26$) or 25% ($Z = 32$) contribution to the free-field decay rate, a peak will be observed with the same width as Lyman α, but emitted over $1/e$ lengths of 14.4 mm ($Z = 26$) or 4.8 mm ($Z = 32$) compared with the production location. Conversely, decays within the foil could experience quenching field-induced E1 and M1 decays, in which case decay could be complete within 0.1 mm (depending on the effective field). The peak occurs at 1.783 3157 Å ($Z = 26$), 1.172 2711 Å ($Z = 32$), or 2.66% and 2.34% of the distance from Lyman α_2 to Lyman α_1 [26].

For a hypothetical $2s$ population of 10% of $2p_{1/2}$, this would yield a 1.2% or 2.5% relative intensity and a 0.85 ppm or 2.7 ppm shift to shorter wavelengths for Lyman α_2 only. This might be a realistic estimate, since any Lyman radiation populated downstream would be observed, while corresponding $2s$–$1s$ photons may pass beyond the detector region. However, the population of the $2s$ level is not given by the above data. The modelling of these lifetimes (later) shows that the radiation far downstream has $2s$–$1s$ and $2p$–$1s$ of near-equal intensities, as the dominant prompt $2p$–$1s$ radiation has already decayed, and both are then augmented primarily by cascades.

8.6. 4*f*–2*p* satellites

Hay and Treacy [52] observed $4f$–$2p$ E2 transitions from the Yrast chain with a branch fraction of 6.1%. This will contribute

---

[1] A. Varney. Private communication. 2000.

to observed Balmer β spectra (if present in our case). Estimates based on $\left(Z\alpha/n^2\right)^2$ scaling also predict these transitions but would expect branch fractions of 0.366% for Fe, 0.554% for Ge, and 1.179% for ref. 52 following p. 184, for ref. 53, and for p. 256, ref. 54). Given experimental uncertainty, theoretical values can be considered, with the uncertainty equal to the estimate.

These transitions have not been tabulated earlier. The $4f_{5/2}$–$2p_{1/2}$, $4f_{7/2}$–$2p_{3/2}$, and $4f_{5/2}$–$2p_{3/2}$ components lie 496.4, 249.7, and −0.906 ppm to the short wavelength side of the two main iron $4d$–$2p$ components, (or 748.8, 378.2, and −1.354 ppm for germanium [41]). These separations are large and partially resolved for the strong components, with $R = 2015$, 4005 and 1335, 2644, respectively. The actual shift is critically dependent on the Yrast contribution to Balmer α and Lyman α (later). Intensity ratios follow expected sum rules and are 7:12:2 in field-free decay. Experimental $4d$–$2p$ ratios show larger $4d_{3/2}$–$2p_{1/2}$ intensity than expected. This is consistent with a contamination of $4d$–$2p$ with $4f$–$2p$, but the ratio of $2p_{3/2}$ to $2p_{1/2}$ is the same in both cases. Fitted values for $4d_{5/2}$–$2p_{3/2}$ versus $4d_{3/2}$–$2p_{3/2}$ are unresolved and would be affected by $4f$–$2p$ locations as well as intensities. Experimental d–p ratios are strongly film-dependent for thin targets, and the uncertainty is larger than the difference between statistical ratios. *The largest uncertainty in systematic shifts from satellite contamination is therefore due to the contributing 2s–1s and 4f–2p satellites.*

8.7. Fitting errors

Systematic fitting errors should be considered. Possible (7 ± 7)% increase in $4p_{3/2}$–$2s_{1/2}$ of the unresolved profile at the expense of a corresponding (21 ± 17)% decrease in $4s_{1/2}$–$2p_{1/2}$ could correspond to a large Balmer β shift (96 ppm). However, this is heavily constrained by the absence of a corresponding effect on Balmer β_1 or β_5, which may be of the opposite sign but are no more than 22 and 15 ppm (PET) or 1σ intensity deviations. Scatter between individual scans is somewhat larger, and this estimate is model dependent. Results for both ADP and PET crystal data are consistent, disproving this as a significant cause. Our estimate in ref. 26 of the possible consequence of profile misidentification, −19 ± 19 ppm, is 2–6 times the standard deviation of the global fitted discrepancies, would include satellite shifts and is of the correct sign, but is far too small to explain the observed structure.

9. C1 Thickness-dependent decay locations

For the fraction of any (Lyman) decay increasing with thickness (in the foil) a shift of the (Lyman) emission source will be upstream compared with that for Balmer radiation. The location upstream of Lyman radiation emitted within the target may be prompt at the exit of the foil (from wake fields) or uniformly excited (and deexcited) throughout the foil thickness. We assumed the latter for this estimate, but show that the error is negligible between these two options because of the thin foils used. If emission arose from halfway through the (9 μg cm^{-2} target), the Lyman α beam energies would be 0.11 MeV higher than Balmer β [31, 32], or $\delta\beta = 1.5\times10^{-5}$, giving $\delta\lambda = 2$ ppm. An additional effect arises for the shift of the dispersion plane for Lyman α versus Balmer β radiation. This corresponds exactly to a shift of the parameter w_0 between the radiation, and because of the slanted lines may be seen as creating a Doppler shift between the radiation [26].

The slant of the lines on the film is approximately β, so this 11.25 μm shift upstream would give a 2.0 μm shift across the film or a 5.7 ppm discrepancy. This latter effect only applies to 23% of the radiation, and hence is insignificant. It would shift Lyman α upstream, giving low Lyman α wavelengths, and would be corrected for by shifting λ to larger values. Wake fields (in the foil or at the exit) may shift relative Balmer intensities, but Balmer transitions do not occur inside the foil [46].

9.1. Cascades and population models

Prompt emission is significant. The thickness-dependent component is emitted in the foil or at the exit and not mediated by cascades (from the small increase in Balmer α with thickness and the absence of high-n thickness-dependent contributions). Given that this component explicitly involves only $n = 2$ and 3 states and cascades, the population mechanism for the other component may be investigated using the bulk of the data.

If the remaining C2 component (independent of thickness) is emitted at the same location as the Balmer β radiation, relative lifetimes lead to shifts of the dispersion plane location w_0 by $\beta\gamma c\Delta\tau$ or a mean shift along the film of $\beta^2\gamma c\Delta\tau$. For PET and ADP diffraction, the Lyman α region yields a 2.28 and 3.65 ppm shift in wavelength per micrometre along the film, respectively. Thus, with $\tau_{\mathrm{Ly}\alpha} = 3.401 \times 10^{-15}$ s ($Z = 26$) and $\tau_{4s,4p,4d} = (147.2, 26.36, 77.6) \times 10^{-15}$ s for Fe ($Z = 26$), effective shifts for this iron experiment defined by $4d$ versus $2p$ values will be 0.41 μm or 0.93 ppm for PET and 1.50 ppm for ADP. This correction would be negligible.

However, any free decay of the $2s$ state will incorporate shifts of 1944 μm, or 4432 ppm, or 7100 ppm (limited by the observation length) for the observed fraction in the Lyman α_2 component! Importantly for the companion paper [26], if the Lyman or Balmer lines arise predominantly from high-n cascades, the production location w_0 of either or both may be shifted downstream and give systematic shifts of this order. Thus, it is essential to understand the fraction of decays occurring promptly versus the component produced after cascaded decay, and to estimate the n-level of the initial production.

9.2. Experimental decay locations and the observation window

A truncation must be performed for radiation emitted more than 2 mm downstream of the target, which is collimated out in the experiment. This is modified in the ADP diffraction data because of the tilt angle and depends on the source location (estimated as 0.8 ± 0.1 mm for A322S and A317A, and 1.5 ± 0.1 mm for B422S and B417A).

A trend exists in the relative intensities of PET spectra taken with the B versus A Rowland circles (each observation included two symmetric circle exposures as discussed earlier and given in the film label, e.g., A1xx or B2xx). Total Balmer β cross sections vary insignificantly (1.8±1.5)%, but the B circle shows stronger

Lyman α, Lyman β, and Balmer γ, δ, ϵ, and ζ by factors of 1.25 ± 0.08, 2.05 ± 0.48, 1.38 ± 0.17, 1.70 ± 0.31, 4.8 ± 2.0, and 3.0 ± 1.6. The ratios are 2–3 σ away from ratios of unity expected here and observed in ADP results. The discrepancy arises from crystal-dependent effects (two different crystals are used simultaneously), likely because of vertical curvature.

This effect is small. The less focused B circle observes decays from further downstream than the A circle, suggesting that Balmer β radiation may be less delayed than the higher Balmer series and Lyman α. Values for the A circle correspond to the 2 mm observation length more precisely. Deformation of the foil by 0.5 mm for spectra was observed for exposures A115C and B415A, which led to an offset for B415 attributable to the radiation source lying downstream. For A115C and B415A, the expected downstream collimation is (therefore) 1.6 ± 0.1 mm. Other targets might expect the 2 mm observation length to be reduced by 0.1 ± 0.1 mm by slight target angles or weak bowing of the target. These results yield a fully consistent data set.

10. Theoretical models for capture and excitation cross sections

Numerous theoretical models have been proposed for relativistic projectile electron capture. Prompt emission and in-foil models are contraindicated by the high-n distribution of decays independent of thickness. As the principal quantum number increases, the lifetime increases approximately as $n^{4.5}$ or as n^3 for a given l. Further, any cascade through Yrast chains and Balmer α will not affect Balmer β lifetimes but will give much delayed Lyman α intensities. Relative intensities for the Lyman and Balmer series gained in these experiments place precise limits on the mechanisms populating ns, np, and nd states. Stark fields would alter populations and decay rates for the thickness-dependent component. The thickness-independent component includes all high-n states, is populated at the foil exit, and should therefore yield field-free decays and cascades.

Simplest capture–excitation models (Oppenheimer–Brinkman–Kramers (OBK) and the first Born approximation high-energy limit) assume statistical population with a n^{-3} total cross section or a $2l + 1/n^5$ relative value for an nl state [55, 56]. For an nlj level, this becomes $2j + 1/2n^5$. Transitions may follow ratios given by statistical population plus cascaded decay.

Discrepancies have been observed between the simple statistical model and experiment [52, 57]. The first-order Born contribution σ_1 accounts for a single scattering process and differs from the OBK method (σ_{OBK}) by including the internuclear potential [58]. The second-order or double-scattering (Thompson) term of the Born series for electron-capture (σ_2) can dominate at high (but not asymptotic) velocities and is expected to be significant in the 10–80 MeV/amu range and for $n > 1$ (our case) [59–62]. Calculations assume a hydrogenic (gas) target but may be relevant to first order. At energies above 20–40 MeV/amu, radiative capture (σ_{RC}) dominates with a different $n(l)$ dependence but mainly for capture to low-lying states. Expansions in $Z_{\mathrm{P}}/Z_{\mathrm{T}}$ or $Z_{\mathrm{T}}/Z_{\mathrm{P}}$, where subscripts P and T stand for the projectile and target (prior or post forms, respectively) treat dominant nuclear potentials to various orders giving the impulse approximation calculated with a continuum-distorted-wave formalism (σ_{CDW}) or with a peaking approximation for the momentum integration (σ_{PIA}) [63–66].

These methods can overestimate cross sections by a factor of ten. The eikonal approximation treats one of the potentials to first order and the other to all orders, and its relativistic form may give more reliable total cross sections (σ_{EA}) [67–69]. Calculations in the OBK formalism have attempted to include effects of a wake or exit field [56, 70]. Other theories usually lack a general implementation and are not discussed here. Good reviews include refs. 71 and 72.

10.1. Theoretical models for electron capture, excitation, lifetimes, and branching ratios

Excitation cross sections must be considered with radiative lifetimes and branching ratios. Lifetimes may be scaled from Bethe and Salpeter or other sources [73–75] with or without consideration of Stark effects.

All processes are considered in various approximations in an excellent series of articles by Anholt, Meyerhof et al. [76–81] including estimates for excitation cross sections; capture and excitation processes are discussed in ref. 55. The excitation cross section for $1s$–n shells is given ref. 77) as,

$$\sigma_{\mathrm{Ex}}(1s, n) = \sigma_0 \int_{\overline{q}_{\min}}^{\infty} \frac{2^9}{3n^3} \frac{3\overline{q}^2 + 1 - n^{-2}}{\overline{q}} \times \frac{\left(\overline{q}^2 + (1 - 1/n)^2\right)^{n-3}}{\left(\overline{q}^2 + (1 + 1/n)^2\right)^{n+3}} S(Z_{\mathrm{P}}\overline{q})\, \mathrm{d}\overline{q} \quad (1)$$

$$\overline{q} = \frac{q}{Z_{\mathrm{P}}}, \qquad \overline{q}_{\min} = \frac{1 - n^{-2}}{2\sqrt{\eta}} \quad (2)$$

$$\sigma_0 = 4\pi \left(\frac{a_0 \alpha Z_{\mathrm{T}}}{\beta Z_{\mathrm{P}}}\right)^2, \qquad \eta = \left(\frac{\beta}{Z_{\mathrm{P}}\alpha}\right)^2 \quad (3)$$

Here a_0 is the Bohr radius and $S(q)$ is a screening correction. The cross section is dominated by the n^{-3} dependence, but the l dependence of cross sections is not given. Excitation within subshells should be large and lead to statistical ratios.

Most improved electron capture models are defined relative to the OBK prediction, which in its asymptotic form is

$$\sigma_{\mathrm{OBK}}(1s - nl) \propto \frac{1}{n^3} \frac{A^{2l} 2^{6l} (l!)^2}{(l + 5)((2l + 1)!)^2} \times (2l + 1) \Pi_{i=0}^{l} \left(1 - \frac{i^2}{n^2}\right) \quad (4)$$

where $A = Z_{\mathrm{P}}\alpha/\beta = 1.40$ (second iron experiment) or 1.31 (germanium data) [61, 68]. This expression is valid for $A/n \ll 1$, not obeyed here except for high n, but may be used as an estimate. The expression for lower n is more complicated (see p. 303 of ref. 72). Both lead to higher l shells being populated for medium and low-n (or lower velocities). For individual m_l target magnetic quantum states, ratios for p_0 to $p_{\pm 1}$ are 12:1:1 and ratios for d_0 to $d_{\pm 1}$ to $d_{\pm 2}$ are 66:(14:14):(1:1).

For highest orbital quantum numbers ($l = n - 1$),

$$\sigma_{\mathrm{OBK}}(1s - nl = n - 1) \propto \frac{1}{n^3}\left(\frac{A}{n}\right)^{2n} 2^{6n} \frac{(n!)^2}{[n(2n+8)(2n-2)!]} \tag{5}$$

$$\sigma_2 - \sigma_1(1s - nl = n - 1) \propto \frac{Z_{\mathrm{P}}^{2n}}{n^3(nZ_{\mathrm{T}} + Z_{\mathrm{P}})^{2n-1}(Z_{\mathrm{T}} + Z_{\mathrm{P}})} \tag{6}$$

$$\sigma_R(1s - nl = n - 1) \propto \frac{1}{n^3}\left(\frac{A}{n}\right)^{2n} 2^{4n} \frac{(n!)^2}{n(2n-2)!} \tag{7}$$

For capture from the 1s target state into a state nlm$_l$, σ_2 has been calculated [61], but approximate analytic asymptotic results are only given for $n = 1$–3. They suggest that $m_l = 0$ sublevels are even more dominant in the capture process than in the OBK formalism. Conversely, CDW models predict cross sections larger for larger m_l for a given l (i.e., statistical subpopulations), and post-eikonal forms ($Z_{\mathrm{P}} \gg Z_{\mathrm{T}}$) predict something similar. The CDW method predicts $1s : 2s : 2p_0 : 2p_{+1}$ at the asymptotic limit in ratios $2^3 16/13 : 1 : 1/104 : 21/416$. The second Born approximation predicts an n^{-3} dependence for high levels in the $\beta \to c$ limit, but the CDW method does not.

These models may be considered qualitatively with regard to l-selectivity. For low velocities, initial capture leads to $l \simeq 1$–2 or to $l \simeq \sqrt{q}$ if a restricted range is involved (for high charge q and n), but rotational mixing of subshells often leads to statistical ratios. In the high-velocity regime, long-range interactions lead to population of high l-subshells, but with further increasing velocity this reverses towards the asymptotic limit where $l = 0$ is again recovered. $m_l = 0$ at low- and high-velocity regimes or $\Delta m_l = \pm 1$ (i.e., $m_l = \pm 1$ for $1s$ capture) in rotational mixing, but the intermediate regime has significant population of nonzero values (as in the CDW model).

10.2. Experimental support from the literature

Hay and Treacy [52] observed high-n decays from Rydberg states excited by 130 MeV Br^{25+} + 20 μg cm^{-2} C targets and concluded that four processes feed the $2p$ state. The standard Yrast cascade through $3d$–$2p$ and the direct $n(s/d)$–$2p$ transitions were observed, as expected. The strongest transition was $3s$–$2p$, fed from the Yrast $4f$–$3d$ transition by trapping (because of the nearly filled $n = 2$ shell). The dependence with decay length implied that initial high-n populations are strongly nonstatistical and decay to Yrast states in a single step (or are initially Yrast-populated only). The direct $n(s/d)$–$2p$ transitions appeared to be 4% of the Yrast contribution. A $4f$–$2p$ E2 transition from the Yrast chain is also observed, with a branch fraction of 6.1%. This would contribute to observed Balmer β spectra (if present in our case).

Experimental and theoretical capture cross sections for heavy bare iron and krypton ions have been given for $1s$ target capture [48, 82]. For carbon targets, $2s$ and $2p$ capture are three orders of magnitude less important *in the OBK formalism*. For 33–34 MeV/amu bare krypton incident on 10–25 μg cm^{-2} carbon or other targets, total Lyman α yields were found to be the same as for gas targets and in good agreement with σ_{CDW} estimates, but Lyman β and γ solid target yields were (30–50)% lower than gas and CDW estimates. The intra-shell $l - l'$ excitation increases as n^4 but was considered too slow to affect an apparent relative increase in high-l substate populations observed from the relative 4–2, 5–2 versus 3–2 intensities. This was attributed to a Stark mixing of l-states for any given m population. Spectra provided therein are similar to solid-state data elsewhere [38, 46, 84] but of lower resolution. Experimental cross-section ratios for 400 MeV bare iron projectiles on nitrogen gas targets were measured and found to give ratios for Lyman α, β, γ, Balmer α, and γ, respectively, relative to Balmer β, of 5.8 ± 0.7, 1.19 ± 0.18, 0.615 ± 0.088, 2.08 ± 0.23, and 0.46 ± 0.06.

This is quite close to the current iron excitation–capture conditions ($E = 480$ MeV, solid $Z = 6$ versus $E = 400$ MeV, gaseous $Z = 7$) and is in good agreement for the Lyman series for the thin targets, given (Sect. 8) that np–$1s$ radiation is unpolarized and nd–$2p$ radiation is π-polarized. Hence, an estimate of Balmer α intensity for the iron experiment may be gained from the mean of these two values.

11. Models tabulated and compared

Given this background understanding, we can model the observed spectra using a range of plausible assumptions to consider whether appropriate theory is available and to conclude the expected magnitude of model-dependent systematics. The second component C2 is modelled with a field-free (radiative) E1 decay model of ref. 83, modified to include $2s$–$1s$ 2-γ and $4f$–$2p$ E2 decays and to allow the following population models:

(M0) the simple asymptotic $0.5n^{-5}(2j + 1)$ statistical model, corresponding to large subshell mixing before decay, *neglecting cascades*;

(M1) population of $l = n-1, n-2, n-3$ states only, including cascades (i.e., almost pure Yrast cascades by capture into high-l Rydberg levels);

(M2) the OBK asymptotic expression in (4), coupled with a statistical redistribution between j values, before decay, including cascades;

(M3) n^{-2} statistical population for $n < 5$ with n^{-3} above this, including cascades, a test of the n^{-3} dependence for medium n and its impact upon relative populations;

(M4) population of $m_l = 0$ levels only, leading to $1/2l+1$ populations for each l, followed by j-mixing before decay, including cascades;

(M5) population of $l = 0$–2 states only, with statistical values, including cascades; and

(M6) the simple asymptotic $0.5n^{-5}(2j + 1)$ statistical model, corresponding to large subshell mixing before decay, including cascades.

Table 3. Hydrogenic iron field-free decay locations downstream of target exit plane: $\beta \simeq 0.1335$, 2 mm observation region, 9 μg cm^{-2} target.

$n' = 14(l+1) - nl$	$1s$	$2p$	$3d = 4d$	$4f$	$5g$	$6h$	$7i$
Decay length (μm)	44.37	130.1	260.3	437.0	661.0	933.5	1255

These choices cover particular lj population extremes. M0 is expected to be poor, since we anticipate the significance of cascade contributions. M1 corresponds to the most asymmetric high-l population model it is reasonable to postulate, and we expect that this extreme will also be far from the experimental situation. M2 gives the sharp $l = 2$ peaked distribution, representing the standard reference model. The n^{-3} dependence is retained in all cases except M3; the n^{-3} dependence is certainly expected to be valid for high n, and the correct distribution should lie between n^{-3} and M3 for medium n. Hence, M3 tests the distribution of intensity due to differential population of medium-n states. M4 may represent some Stark models (a wake-field-like model), and M5 and M6 represent (statistical) velocity limits. The purpose is not to discover the excitation model as one of these models, which may vary from one extreme to another from low- to high-n states, but to understand the downstream decay pattern and to isolate contributing processes. For example, Stark effects *may in principle* be important for a region of high-l intermediate-n states only, and statistical redistribution *might* be dominant for high-n states only.

Levels up to $n_{\max} = 14$ are considered; above this level, contributions from $l > 6$ states within the observation length are negligible (and computing time scales as $n^4_{\max}$). For iron, Yrast contributions to $4f$ states via $5g$ are given adequately. We discuss this detail in our conclusions.

Direct population of $4f$ by $15g$ etc. has a decay length of 537 μm and is therefore not included. Coverage of the maximum 2 mm range for these direct decays (of apparently low probability) could require calculations up to $n = 29$. Direct population of $4d$ states from $14f$ and $14p$ states have (field-free) decay lengths of 260.3 and 44.37 μm. Mean locations obtained are weighted towards short-lived states (Table 3). Rates are faster for $14d$–$2p$ (decay length 130.1 μm) so the possible omission of higher n population is more severe for such d–p decays, and a full calculation could require inclusion of states up to $n = 44$.

However, these contributions, although model-dependent, may be calculated by a direct summation and are 5 to 7 times the $n = 14$ contributions (assuming an n^{-3} dependence). In the statistical model, they give additional 0.13%, 0.30%, and 0.35% contributions to $4f$–$2p$, $4d$–$2p$, and $2p$–$1s$ C2 component intensities, all of which are long-lived and emitted ca. 900, 800, and 700 μm downstream, respectively (the value for $2p$–$1s$ is corrected for the observed intensity ratio). They have a minor 1–3 μm contribution to the mean decay location, but this could be greatly increased if $n = 2$–4 states fail to observe statistical population ratios (i.e., if they are particularly weak). Other two-step decays to relevant levels are less important and may be neglected.

Multiple-electron satellites have been shown negligible for thin foils in Sect. 8. The dispersion relation has been used (for nd, p, s–$2p$, s), assuming a common source location for all Balmer components for a given upper principal quantum number. Models imply that source shifts of 10–30 μm up or downstream are expected for certain weak Balmer β and γ components, corresponding to 2–5 μm along the film or 1%–3% of the fwhm of the peaks. With the exception of $4f$–$2p$ (and $2s$–$1s$) transitions, this will not affect identifications or intensities.

11.1. Discussion of model agreement and relevance for field-free decay

Table 2 shows clearly that cascade effects are dominant and necessary to explain relative intensities, and that relative intensities are strongly model-dependent for the initial populations. The main assumption common to all models is that the E2, 2E1, M1 processes and Stark effects are not significant in decays and cascades (except for $2s$–$1s$ and $4f$–$2p$ transitions). This is confirmed by experimental branching ratios for $3p$–$1s$, $4p$–$1s$, and $5p_{3/2,1/2}$–$1s$ versus nl–$2s$ transitions in Balmer α, β, and γ. Unresolved Balmer α provides an upper limit to the Lyman β intensity. Lyman β component ratios are consistent within a factor of two.

Balmer β and γ component intensities also confirm field-free branching ratios. Iron Balmer γ ratios and $4s$–$2p_{1/2,3/2}$ are in good agreement. Iron $4d_{3/2}$–$2p_{1/2,3/2}$ ratios also agree but may be slightly contaminated by $4f$–$2p$ or subject to fitting errors. Thus, branching ratios appear valid for $n = 3$–5 states.

11.2. Discussion of model agreement and relevance for high-*n* states and cascades

M0 neglected cascades and hence should be expected to fail for high-n transitions such as Balmer δ ($6l'$–$2l$) or Lyman δ ($5p$–$1s$). It certainly does, but it also fails completely in predicting the ratio of intensities of Lyman α to Balmer β. Cascades must be included to evaluate the observed intensities of even the lowest-lying intensities and in particular the Lyman α to Balmer β ratio.

M1 only includes Yrast-like cascades, and comparison with data estimates the significance of these processes in feeding the lower levels. This model consistently underestimates all Balmer series intensities, and where Balmer γ and Balmer β are fitted with multiple components, only three or four of these components have reasonable values. Lyman γ, β and α are all strong in this model, so these transitions may be fed significantly by cascade contributions. M1 is poor for levels above $n = 5$ (where s–d states are not fed by $l = n - 3$ to $l = n - 1$ states) but gives (accidental) close agreement for iron $5d$ populations, suggesting that high-l population cascades might significantly contribute to Balmer γ.

M2 is the OBK model, known to require modulation as given in more recent theoretical development but which might be considered to be far superior to models M3, M4, M5, M6. It is not. It clearly fails in the high-n region and implies that the classical $l = 2$ peaking is not significant in the population of higher

n states. The predicted d-state peak is *not* observed. This approximation may have value in lower n shell populations (see below) but makes little contribution to an evaluation of the overall contributions to cascades and significant downstream decay shifts.

In this high-n region, the remaining models divide sharply. M3 gives the monotonic statistical ratio but with increased effect due to the higher relative high-n populations; M4 gives an l-independent distribution; M5 includes low-l "direct" cascades only, which are a small contribution to the total for low levels; M6 gives the monotonic statistical ratio.

M3 overestimates intensities above $n = 5$ by a factor of two or three. To investigate the models directly in this high-n region, we could normalize all intensities to the (weak and less well-determined) Bamler δ_5 intensity. To repeat this would be repetitious, so we summarize the comparisons instead. If applied to M3, this yields almost exactly the model of M6, since they have the same assumptions above $n = 5$, but of course the test of M3 is the comparative agreement for he $n = 5$ populations and hence for the Balmer γ and Lyman δ peaks. This is where we find proof that the n^{-2} dependence is not valid for $n = 5$ states and that n^{-3} dependence *is* approximately valid at least down to $n = 4$ in these regimes.

M4 predicts intensity ratios in disagreement with both experiments and overestimates high-n intensities by 50%–100%. There is a tendency for the Balmer 1–4 components to be overestimated by a factor of 2.5, while the Balmer 5–7 components are overestimated by approximately a factor of 1.5. This is inconsistent with any renormalization of intensities. We have noted that branching ratios follow a field-free decay model, subject to uncertainties. This result suggests that the effect of possible strong Stark or wake fields are not observed in these data. The conclusion does not say that such fields do not exist, only that they are not strong enough to dominate or have a significant effect in this regime. This result also confirms that the $m_l = 0$ level population mechanism is not dominant for medium or high n.

M5 and M6 are both statistical models. Both agree well for all Balmer series above and including Balmer γ, without the need for renormalizing to Balmer δ_5. Without this normalization, M5 yielded three intensities that were 3–4 standard deviations from experiment, with another three from 1.5 to 2 σ (these were however generally the strongest and hence most reliable intensities). Similarly, for M6 there are three intensities that were 3–4 standard deviations from experiment, with another 2 from 1.5 to 2 σ (these were however generally the weakest and least reliable intensities).

M5 tends to overestimate observed intensities for transitions from $n > 5$ upper levels (the normalization to Balmer δ_5 would reduce the intensities by a factor of 1.4 ± 0.1), which is significant for iron. Conversely, the normalization to Balmer δ_5 for M6 would reduce the intensities only by a factor of 1.1 ± 0.1. With this normalization (i.e., comparing only the high-n transitions), the number of significant discrepancies for M5 increases to yield three intensities with 3–4 standard deviations from experiment but another 6 from 1.5 to 2 σ. Incidentally and interestingly, the dominant discrepancies for both models (with or without normalization) are all in the Balmer γ and Balmer δ series; the weaker intensities of the higher series are less able to discriminate between such similar models.

The identification of partially resolved components of Balmer multiplets is unaffected by the variation in decay location due to differential component lifetimes. The separation in decay lengths for the Lyman doublet components are neglible in all models. Subject to fitting uncertainty, the typical shift in expected decay length between Balmer components is ca. 20 μm, corresponding to a 10 ppm apparent energy shift. This may be compared with, for example, separations in energy of 497 ppm between Balmer δ_5 and Balmer δ_7 or 126 ppm between Balmer δ_5 and Balmer δ_6 (and larger relative separations for Balmer γ and Balmer β components). Hence, component intensity identifications are robust.

M5 therefore overestimates s-state populations, as expected, but also overestimates d-state populations. M6 may slightly underestimate high-n p-states. Experiment suggests that $l = 0$–4 states give dominant contributions to high-n Lyman and Balmer series, and that the distribution is near-statistical but perhaps weakly peaking around d–f states. f-state contributions are significant but may be slightly weaker than $2j + 1$ would suggest.

The cascade contribution from high-l populations (following the M1 model) is only observable in Balmer γ (and lower n) transitions and is dominated by the $6f$ and $5d$ populations. M1 also only includes pure Yrast decays versus immediate collapse modes included in M6. Both M6 and M1 are consistent with Yrast observations [52], but direct cascades (from M5) accounted for 4% of the total, suggesting near-statistical l-state distributions, especially in the high-n states.

The Lyman series limit cannot discriminate between models, but the Lyman δ ($5p$–$1s$) intensity, admittedly with large uncertainty, favours the directly statistical model M6 rather than M5 (or other models).

Therefore, the decay locations of $n = 5$ transitions and above are given reliably in Table 4, column C2, by the values computed for model M6 with a relatively small uncertainty.

11.3. Discussion of model agreement and relevance for $n = 4$ states

Capture into s-substates is predicted to be small in the main theories (CDW, PIA, etc.) in the iron beam energy range, and CDW calculations predict $\sigma(1s - 3s)/\sigma(1s - 3) = 0.04$ and $\sigma(1s - 4s)/\sigma(1s - 4) = 0.03$ [48]. By comparison, M1 gives 0, the OBK model M2 yields 0.031 and 0.021, M4 gives 0.33 and 0.25, statistical models (M6, M3) give 0.056 and 0.031, and M5 gives 0.056.

M2 (OBK) predicts small $4f$ and $5g$ populations and $5d$:$4d$:$4p$ ratios in rough agreement with CDW and PIA methods. OBK predicts a sharp peak for d-state populations for a given n, compared with statistical monotonic increases and the extremes of M4–M1. Our experimental results agree more closely with M1, M3, and M6 for Lyman γ and Balmer β $4p$ estimates and for Balmer γ $5d$ estimates. Both suggest that CDW, PIA, and M2 overestimate $4p$ and $5d$ populations by 42%–51% and 110%–45%. This is a partial justification for not pursuing these more complex models further, in rough agreement with other solid target observations.

Table 4. Hydrogenic iron decay locations downstream of target exit plane: 2 mm observation region, 9 μg cm^{-2} target, $\beta \simeq 0.1335$ (results in μm). Note that M0 and M1 are completely inconsistent on the basis of Table 2 and therefore are not used further.

	Model predictions							Limit Prediction	
Line	M0	M1	M2	M3	M4	M5	M6	C1	C2
Ba 7_{5-7}[a]	35.05	785.2	43.68	44.89	44.59	35.13	44.89		44(2)
Ba ζ_{1-4}	24.24	386.2	33.18	35.11	33.85	24.32	35.11		35(2)
Ly γ	1.070	1.683	10.21	17.78	9.571	3.929	5.55		5.5(5)
Ba ζ_{5-7}	24.74	395.9	34.96	35.65	35.82	24.82	35.65		35(2)
Ba ϵ_{1-4}	16.32	153.9	26.71	28.29	27.36	16.40	28.29		28(2)
Ba ϵ_{5-7}	16.68	159.0	28.54	28.68	29.45	16.76	28.68		28(2)
Ba δ_1	10.34	47.48	22.32	23.82	23.27	10.43	23.82		23(2)
Ba δ_2	3.554	53.40	11.24	8.908	14.73	8.254	8.908		8.5(5)
Ba δ_3	47.39	102.4	50.86	47.73	47.79	47.72	47.73		47.7(5)
Ba δ_4	3.557	51.05	8.740	8.945	9.971	8.293	8.945		8.9(5)
Ly β_1	0.458	2.481	11.13	26.79	9.180	2.404	6.106	−9.67	6.1(5)
Ly β_2	0.459	2.484	8.227	26.85	6.056	2.425	6.142	−9.67	6.1(5)
Ba δ_5	10.59	49.14	24.25	24.10	25.64	10.67	24.10		24(2)
Ba δ_6	10.34	47.48	22.32	23.82	23.27	10.43	23.82		24(2)
Ba δ_7	47.39	102.4	50.86	47.73	47.79	47.72	47.73		47.7(5)
Ba γ_1	6.036	9.777	19.91	52.21	22.36	6.113	22.57		22(2)
Ba γ_2	2.070	12.49	10.38	18.81	11.86	5.873	6.840		6.8(5)
Ba γ_3	31.21	44.29	35.02	32.69	31.65	31.53	31.54		31.5(5)
Ba γ_4	2.073	11.93	7.776	18.86	7.828	5.905	6.870		6.9(5)
Ba γ_5	6.190	9.941	22.01	52.49	25.38	6.268	22.77		22(2)
Ba γ_6	6.036	9.777	19.91	52.21	22.36	6.113	22.57		22(2)
Ba γ_7	31.21	44.29	35.02	32.69	31.65	31.53	31.54		31.5(5)
$4f_{5/2}$-$2p_{1/2}$	6.382	126.0	42.16	278.0	151.7	16.90	149.1		150
Ba β_1	3.118	15.20	19.63	81.26	28.54	3.191	28.76		31
Ba β_2	1.070	1.683	10.21	17.78	9.571	3.929	5.537		6
Ba β_3	20.10	21.93	24.34	21.77	20.58	20.40	20.42		21
Ba β_4	1.072	1.682	7.500	17.80	6.254	3.955	5.564		6
Ly α_1	0.138	15.79	14.29	111.6	23.96	1.287	19.86	−9.99	102
Ly α_2	0.140	15.82	10.89	113.2	16.15	1.303	19.95	−9.99	102
2s–1s	14368	976.9	979.9	978.5	977.2	976.9	977.0	−9.99	978
$4f_{7/2}$–$2p_{3/2}$	6.450	126.1	44.69	278.2	165.2	17.17	149.2		150
$4f_{5/2}$–$2p_{3/2}$	6.382	126.0	42.16	278.0	151.7	16.90	149.1		150
Ba β_5	3.210	15.30	21.99	81.45	33.48	3.284	28.88		31
Ba β_6	3.118	15.20	19.63	81.26	28.54	3.191	28.76		31
Ba β_7	20.10	21.93	24.34	21.77	20.58	20.40	20.42		21
Ba α	1.374	55.21	24.98	200.2	79.99	1.432	69.29	−8.76	80[b]

Note. C1: Possible shift of C1 population source versu foil exit; C2: decay location of C2 components (maximal $2p$ population); M0: result of statistical population, free decay, neglecting cascades; M1–M6: models in text, including cascades ($l = n - 1 \rightarrow n - 3$); OBK; n^{-2} and n^{-3}; $m_l = 0$; $l = 0 - 2$; and statistical).

[a] Tabulated decay lengths are for the dominant multiplet component.

[b] Si(Li) detector results.

Hence the statistical model appears to do well (best) for $n = 4$ states, including the Lyman γ intensity $4p$–$1s$ and particularly for the Balmer β component intensities. In the Balmer β component intensities, statistical models M3, M5, and M6 all predict similar direct population of these states (remember the component intensities are normalised to the Balmer β_5 component). These models differ in the fraction and distribution of cascades feeding these $4s$, $4p$, and $4d$ levels. For cascade contributions to $4s$, $4p$, and $4d$, M5 is disproven by experiment, while M3 and M6 have similar levels of consistency. However, M6 is favoured by the data for Lyman γ.

M6 generally disagrees with experiment by less than two standard deviations. For iron, the key exception is correlated and due to the $4s$ decays, which (as explained above) are overestimated by 40%–60% with M6. This is consistent with other results [38, 46, 84]. $4s$ decays are weak with large downstream shifts compared with adjacent components, but the correlation is not due to statistical modelling or to Lyman α tails (ADP), which affect $4p_{1/2}$–$2s_{1/2}$ more. There may be slight absorption of the two peaks by $4p_{1/2}$–$2s_{1/2}$ and $4d_{3/2}$–$2p_{3/2}$, but these latter intensities agree with model prediction at the 1σ level. Allowance for $4f$ transitions increases agreement for $4p_{3/2}$–$2s_{1/2}$

peaks, and the only sign of peak absorption (of $4s_{1/2}$–$2p_{1/2}$ by $4p_{3/2}$–$2s_{1/2}$) can easily explain the 7%–8% excess of β_2 versus β_4 and simultaneously the 21%–24% deficiency of β_3 versus β_7. Field-induced decay would increase β_2 versus $\beta_{1,6}$, or $\beta_{3,7}$ versus β_4 and is not observed. Mixing of $j = 5/2$ levels may lower β_5 wavelengths only but is also not observed. The remaining observable effect (a 2%–4% or 1σ $4d_{3/2}$ versus $4d_{5/2}$ excess) may be due to $4f$ contributions, slight model deficiencies for d-states, or absorption by the β_6 component. The latter can explain less than a 1% shift, the former is at the 1%–2% level, and omitted direct cascades are at the 0.3% level. These may all contribute, with a component due to the nonstatistical population of these states.

The decay locations of $n = 4$ transitions are therefore also given in Table 4, column C2, by model M6, with a slight modification for the 4*s* initial population (leading to longer decay lengths but with not a large change as the main transitions cascading to the 4*s* are fast), with slightly larger uncertainties. The decay location for the next closest match (M3) is somewhat anomalous, as that model should be corrected for the n^{-3} dependence for $n = 4$. This prescription also provides reasonable estimates for decay locations of $4f$ transitions.

11.4. Discussion of model agreement and relevance for $n = 3$ and $n = 2$ states

The statistical models fail for $n = 3$ populations, implying much less direct population than most models. The cascade feeding populations for Yrast levels and direct 14*l*–3*s*, *p*, *d* transitions have been previously determined, so any excess population is affected by uncertainty in the direct population prediction.

With PIA and CDW, M2 also predicts the lowest population of $n = 3$ levels but with large population of the 3*p* state. Experiment for $n = 2$, 3 iron transitions shows that M2 and M3 models are most relevant but with Lyman α 0.436 times as strong as the M2 prediction, and Balmer α in agreement with M3 and 0.574 times the M2 (and CDW, PIA) predictions. M2 predicts smaller 2*p* populations than models M3, M4, and (M6,M5,M1), but larger values than CDW, PIA, and OBK1 by up to a factor of two.

These dependencies and observed ratios are in reasonable agreement with ref. 48. Hence, 2*p* and 3*p* populations appear best given by CDW and PIA models, but 3*d* populations are then overestimated by a factor of two. This overestimate of initial 2*p* and 3*d* populations in the models then underestimates contributions from cascades to Lyman α and hence yields Lyman α decay lengths too small by approximate factors of 2, 2.8, and 5 for models M2, (M3, M4), and (M6, M5, M1), respectively.

This conclusion for $n = 2$ and 3 populations is then presented in column C2 of Table 4 as the best estimate from experimental data and the pattern of intensities. This correction of the model is only weakly dependent on the cascade fraction. However, the total decay location shift is dictated by the location of the Lyman α decay, which in turn is dictated by the factor of suppression of the direct population. Hence, if the direct decays were suppressed by an additional factor of two, the decay location for Lyman α would be significantly further downstream. These corrections are necessary to include cascade contributions from upper levels for the mean decay lengths.

11.5. Lyman component ratios

Previous investigations of Balmer and Lyman relative intensities have attributed claimed nonstatistical intensities to Stark field decay. We have shown that branching ratios are insignificantly affected, and that intensities require no Stark effects for their explanation. Decays appear to be downstream of the target, avoiding wake and exit fields.

Lyman α and Lyman β C1 components can occur within the foil, which are the only Lyman lines for which components are separately measured. Lyman β is not fully resolved. All the models presented predict ratios between 2:1 and 1.2:1 for iron and germanium, for both Lyman α_1:Lyman α_2 and for Lyman β_1:Lyman β_2. Note that these models do not consider population of Stark mixed states. Statistical models (apparently valid for Balmer β and higher n radiation) predict 2:1 ratios. Experiment observes 2.15 ± 0.07:1 for iron (noting that any result from circa 1.4:1 to 4:1 may be obtained if poor photographic linearization is used). These ratios are consistent with statistical ratios, but thicker foils show the ratio increasing with thickness in both experiments. Tabulated values for Lyman β ratios are 2.28 ± 0.60:1, increasing with thickness.

The 2*s*–1*s* intensity is predicted to be large in all models, with the best estimates of 2.5%–5% contamination of Lyman α_2 for iron (assuming similar suppression of 2*s* and 2*p* levels). Mean decay lengths are very far downstream (970 μm) and yield a fwhm along the film of 262 μm. This will add a contribution of approximately double the observed width, reduce the peak by a factor of two, and shift the centroid downstream of Lyman α_2 by 87.4 μm (PET) or 99.1 μm (ADP). This assumes a 2 mm observation region; for 1 mm, these shifts become 21.4 μm and 33.1 μm, respectively. Using the M2 estimate gives a total Lyman centroid (α_2) displacement of only 1.2 and 3.0 ppm in the 1 mm case. Hence this "additional" contribution, despite its very large displacement of decay location and its presence around the Lyman α_2 component, does not cause a major systematic error in any calibration measurement.

The intensity and location displacement between Lyman β and Balmer α is consistent with a *p*-state versus *d*-state dependence, but the C1 component could be due to *exit excitation* rather than in-target de-excitation (a shift of 10 μm downstream for a small component), and the C1 fraction has significant uncertainty.

The C2 predictions have an uncertainty dominated by the initial 2*p* population correction to the statistical M6 model and the Yrast contribution. The C1 component (increasing with thickness) is small for the thin targets and could have a Lyman α distribution model somewhere between those given for M1 and M3. The M1 model would reduce C2 shifts by 7 ppm, the magnitude increasing with thickness to give no overall effect for 50 μg cm^{-2}, while an M3 prediction would not affect the shifts significantly, depending again on the initial 2*p* population.

11.6. Balmer contamination by $4f$–$2p$ decays

The $4f$–$2p$ decay locations depend on the Yrast contribution rather than initial populations. This is particularly model-dependent, since convoy electrons *may* capture directly into Yrast states, which would only affect Lyman α, $3d$–$2p$, $3d$–$1s$, and $4f$–$2p$ contributions. This may contribute to the thickness-dependent C1 distribution. The models predict that observed $4f$–$2p$ peaks will lie on the short wavelength side of the two strong $4d$–$2p$ peaks by 458.9, 214.0, and -36.6 ppm for PET, and 436.9, 191.8, and -58.8 ppm for ADP diffraction.

The fraction of $4f$–$2p$ in the Balmer spectrum might be 0.82%, 1.12%, and 0.14% for iron compared with the nearest strong peak (from model M6, neglecting additional pure Yrast decays). These estimates will lead to 3.8–6, 2.4–2, and (-0.05)–8+ ppm shifts for iron Balmer transitions. However, these transitions are not definitively observed and the fractions could easily be a factor of five times smaller (i.e., negligible) if the population followed the OBK model M2 for example.

Predictions for Lyman α follow therefore from corrected M6 values with largest uncertainties from the Yrast contribution, the possibility that the C1 fraction may be overestimated, and the uncertain C1 decay location.

12. A consideration of spectral widths, Yrast limits, and Lyman β energies

A detailed consideration of broadening mechanisms and widths confirm several of the conclusions based on relative intensities given earlier [38]. This includes confirmation of the experimental beam divergence and the ideal focussed energy of the beam (in the Balmer η region) and broadening due to straggling in the thicker targets. Straggling therefore appears insignificant for thin targets, and the widths also support the absence of significant Stark effects in the data.

These (surprising) consistencies point to the precision of alignment and focusing and to the utility and accuracy of the diffraction modelling. They also provide a limit to broadening from other sources. The effects of $2s$–$1s$ and $4f$–$2p$ can be revealed more by profile asymmetries than width effects. Profile width shifts are not unambiguous. However, the C2 and Yrast components can broaden spectra dramatically and can therefore be observed or constrained by such an investigation.

If Yrast processes above $n = 10$ were solely responsible for the Lyman intensities, the 2 mm observation length would give a fwhm broadening of 262 μm. This is much larger than the expected decay widths downstream. Quoted results from C2 components (Table 4) would yield width contributions on the film of 17.2 μm, well within the observed 100 μm width and the 75 μm uncertainty. This yields an upper limit to the mean Lyman (or Balmer) decay location of approximately 550 μm. This does not constrain the Yrast limits estimated here but supports the possible magnitude of the corrections.

12.1. Limitations of the $n_{\max} = 14$ modelling cutoff

The mean decay location converges slowly with increasing n, and quoted decay lengths (from the $n_{\max} = 14$ cutoff) are low estimates for Lyman α. Inclusion of $n = 15$–16, with upper level decay lengths of 5.9–8.2 mm or Yrast locations of approximately 17.7–25.9 mm (and hence an average 1 mm in the truncated 2 mm observation region), shifts the mean location from 286.5 to 312.5 μm or by 9%. The value $n_{\max} = 30$ yields 354.0 μm, while inclusion of direct decays from these to $n = 4$ lowers this to 208 μm (compared with the estimate of 101.9 μm based on model M6). These uncertainties are quite large, but the limits from the earlier analysis remain robust.

12.2. Yrast limit derived from relative intensities

Additional Yrast population of $n > 4$ and $l > 3$ states (and mainly $l = n - 1$) would primarily affect $2p$–$1s$, $3d$–$1s$, $3d$–$2p$, and $4f$–$2p$ transitions and cannot be ruled out by the data. Any population of this type would yield equal additional Lyman α and Balmer α intensity, with additional Lyman β at the 1% level and $4f$–$2d$ transitions at the 0.5% level, all arising from essentially the same source location. This could account for 80% or more of the iron Lyman α intensity, depending on polarization and efficiency corrections. This upper limit to the (C2) decay location for Lyman α is a tighter constraint on the populations and decay locations than the discussion of broadening and widths.

12.3. Lyman β $3l$–$1s$ wavelengths and $2p$–$1s$ Lamb shifts

A final critical piece of evidence for populations and models arises from the Lyman β spectra. Lyman β components are not fully resolved but have been fitted locally with Balmer δ and the dispersion relation. These local measurements are consistent with Lyman β having similar source-dependent corrections and discrepancies as Lyman α but do not include (minor) satellite and high-precision diffraction corrections. They do not separate the C1 and C2 components, so are subject to possible systematic shifts due to fitting uncertainties for the partially resolved Lyman β_2 and Lyman β_1 components, for the Balmer δ components, and local dispersion parameter uncertainty. The magnitude of $3d$–$1s$ might give a significant shift in addition to the source location correction, which should only be similar to that for Lyman α in the Yrast model. Typical discrepancies of Lyman β and Balmer δ spectra from the global dispersion relation are small, less than 25 μm.

Lyman β appears to lie below the expected centroid location from global calibration fits. This may be quantified in the PET data to give a mean shift of Lyman β versus α from diffraction, $3d$–$1s$, and source location effects, which are not dependent on local dispersion or Balmer δ errors. Correction for $3d$–$1s$ is similar to the $4f$–$2p$ correction, so should not give a relative shift from Balmer β values; $3s$–$1s$ may be ignored; diffraction corrections should be similar; satellites should occur at a similar low level; and the Balmer fitting error is the same.

The best data set (B220B) yields a shift of Lyman β_1 to shorter wavelengths by 27.49 ± 10.4 μm on the film or upstream by 202.4 ± 76.6 μm if all is due to the source location (for further details see ref. 38). Other data sets are consistent with larger statistical uncertainty. The source location for Lyman β is expected (from decay modelling) to lie 25 μm upstream of Balmer radiation, rather than downstream, and this estimate is not strongly dependent on the Yrast contribution. Thus, Lyman β radiation is expected to lie 42.7 ppm lower than the global fit, and the difference observed provides a second confirmation of the impact of additional Yrast decays. Lyman β wavelengths should (and are) therefore reduced by 37.4 ppm. The corresponding correction factor to the final Lyman α Lamb shift discrepancies (due to the same Yrast contributions) is -29.37 ± 23.8 ppm for PET diffraction [26]. ADP diffraction uses a reduced observation length, so the ADP correction should be less than this. The same scaling as the Yrast limit calculation discussed earlier gives an ADP correction of -23.50 ± 19.0 ppm. The shift is not as low as the Yrast limit given earlier, implying that this final observation and uncertainty agree with the model-dependent and model-independent limits and uncertainties discussed earlier.

13. Summary of observed processes

Further serious attempts to interpret and understand absolute or relative intensities in Lamb-shift measurements should be made, and future experiments should address this issue in a carefully controlled manner. Nonetheless, several separate processes have been identified and partially quantified.

Carbon–carbon bond lengths are 1.4 Å in graphite. Decay lengths for Lyman α are greater than 1000 Å, so any decays inside the foil must have small mean orbital radii to be stable to collisional ionization for a significant fraction of their lifetime. 4s states in iron have mean radii of 0.488 Å. Any larger radius orbitals are likely to be perturbed and collisionally ionized or de-excited before radiative emission. 2p levels have radii of 0.102 Å and 0.083 Å, so should be much less affected by this. It is therefore expected that high-n states cannot decay inside the foil, but that 2l, 3l (and perhaps 4l) states may. This prediction depends on precise electron distributions. Results suggest that this in-target production process occurs for 2l and 3l, but not significantly for 4l states. Dominant noncollisional processes inside the foil are thus 1s–(1s–3l) hydrogenic capture and de-excitation. There is evidence that this (C1) component yields nonstatistical Lyman α and β ratios. This component may include exit excitation of these hydrogenic states to Yrast states (possibly via convoy electron production), leading to thickness-dependent 4f–2p, 3d–1s, 3d–2p, and 2p–1s contributions.

High-n helium-like (and lithium-like) states, neglecting double-capture processes, are only produced by the capture of electrons by hydrogenic ions or excitation of helium-like 1s(1–3l) states at the foil exit. These are proportional to target thickness and explain the dependence observed. This experiment does not investigate the region approaching equilibrium where multiple capture, straggling, beam energy loss, and wake fields may play more significant roles, but where the resolution of spectra and the separate identification of components becomes (much) less secure.

The thickness-independent component of hydrogenic spectra is produced by a combination of foil-capture-with-exit-excitation and exit-capture processes. Initial populations might involve Stark mixing, but decays are in field-free regions.

13.1. The observed population model

The population process is markedly nonstatistical for $n < 5$ and follows complex capture models for the dependence in this region, but is consistent with n^{-3} and statistical populations for $n > 4$, with s-state populations reduced by 40%–50% and with a possible weak peaking for d–f states. This may be due to rapid redistribution, radiative capture of convoy electrons, or other processes.

In relation to possible source location shifts, the simple statistical model (M6) may therefore be corrected for these lower ($n = 2$–4) 2s, 2p, 3s, 3p, 3d, and 4s initial populations to compare cascade-dependent contributions from medium and high-n levels, as presented in Table 4.

Lyman radiation appears to be unpolarized, and Balmer β (nd–2p) radiation appears significantly π-polarized with oscillation along the beam axis. Decay lengths and source locations may be estimated from these models, allowing relevant shifts of Lyman α with respect to Balmer β to be quantified and allowing estimation of hydrogenic contamination of these peaks. Fitting-dependent shifts of measured peaks have been quantified. The Yrast contributions are less well-defined and are most amenable to future measurement. Contributions from high-n states are dominated by the Yrast component, by direct population, or by immediate collapse of initial states.

The C1 process contributes minor additional shifts between the determined energies of Lyman and Balmer series spectral peaks, as given in Table 4: the decay locations for all thickness-dependent fractions are almost equal in all models, whether this is due to the wake field or simply to the direct production of excited states within the foil. However, the dominant shift in relative decay location is due to the field-free downstream decay of the observed initial population distribution, and this must therefore be modelled carefully.

Remaining concerns and discrepancies suggest some additional role for very high-n population ($n > 14$) and Yrast population mechanisms (population of $n > 4$, $l > 3$ states and mainly $l = n - 1$), which could certainly not be observed directly but can be imputed from measured transitions via modelling. These additional processes may likely be due to capture from wake electrons at the exit or in field-free regions downstream. There is of course significant uncertainty in quantifying these last two processes, but it is possible to gain a specific consistent conclusion regarding the effect of the Yrast contributions, in particular upon the overall populations and the decay locations.

The combination of decay modelling and high-resolution spectroscopy make extremely powerful tools for monitoring and diagnosing plasma dynamics and for selecting and optimizing conditions for particular experiments. In this case it also allows a detailed comparison of data to a range of relativistic theories, and points to limitations in the assumptions made in statistical and nonstatistical state distribution models.

We have proved

(*i*) that there are clearly separable thickness-dependent and thickness-independent components of given spectral lines in thin-target beam-foil spectroscopy,

(*ii*) that the components generated inside the foils appear constrained by bond lengths to be low-n,

(*iii*) that the thickness-independent components appear to decay in a field-free regime,

(*iv*) that a variety of models fail to account for the detailed distribution, but that a well-defined model can be defined based upon theoretical principles, which is strongly supported by the data,

(*v*) that the high-n, high-l populations are significant and cannot be neglected, and that Yrast cascades and similar processes are required to explain the data,

(*vi*) that upper levels appear populated at close to statistical distributions in this relativistic regime,

(*vii*) that the radiation appears to vary in polarization (especially Balmer β compared with Lyman α), and

(*viii*) that contamination by multi-electron transitions is generally negligible in this "single-electron capture" regime from bare Fe^{26+}.

We did not assume the absence of contamination, and in particular have assessed in detail the contribution of dielectronic satellites, Lyman γ, $2s$–$1s$, and $4f$–$2p$ components that have generally been neglected in earlier analyses. We find that their contributions are small compared with other factors.

Acknowledgment

The author gratefully acknowledges the team involved in the original data collection and especially J.M. Laming, D.D. Dietrich, W.A. Hallett, R. McDonald, and J.D. Silver.

References

1. L. Kay. Phys. Lett. **5**, 36 (1963).
2. S. Bashkin. App. Opt. **7**, 2341 (1968).
3. S. Bashkin, L. Heroux, and J. Shaw. Phys. Lett. **13**, 229 (1964).
4. A.K. Dupree, P.V. Foukal, and C. Jordan. Astroph. J. **209**, 621 (1976).
5. D.C. Morton. Astroph. J. Supp. Ser. **130**, 403 (2000).
6. H.G. Berry, L.J. Curtis, D.G. Ellis, and R.M. Schectman. Phys. Rev. Lett. **32**, 751 (1974).
7. M.R. Tarbutt, R. Barnsley, N.J. Peacock, J.D. Silver. J. Phys. B, **34**, 3979 (2001).
8. S.M. Younger, W.L. Wiese, and E.J. Knystautas. Phys. Rev. A, **21** 1556 (1980).
9. H. Gould and T.M. Miller. Adv. At. Mol. Opt. Phys. **51**, 343 (2005).
10. I.A. Sellin and D.J. Pegg (*Editors*). Beam-foil spectroscopy. Vols. 1 and 2. Plenum, NY. 1975.
11. E. Beimont, H.P. Garnir, P.-H. Lefebre, P. Palmeri, L. Philippart, P. Quinet, D. Rostohar, and C.J. Zeippen. Eur. Phys. J. D, **40**, 91 (2006).
12. E. Träbert. Can. J. Phys. **80**, 1481 (2002).
13. E. Biemont, P. Palmeri, P. Quinet, Z. Dai, S Svanberg, and H.L. Hu. J. Phys. B, **38**, 3547 (2005).
14. M.J. Vilkas and Y. Ishikawa. J. Phys. B, **37**, 4763 (2004).
15. B. Lin, H.G. Berry, T. Shibata, A.E. Livingston, H.P. Garnir, T. Bastin, J. Desesquelles, and I. Savukov. Phys. Rev. A, **67**, 062507 (2003).
16. A. Lapierre and E.J. Knystautas. J. Phys. B, **33**, 2245 (2000).
17. H. Gould, R. Marrus, and P.J. Mohr. Phys. Rev. Lett. **33**, 676 (1974).
18. C.T. Chantler, D. Paterson, L.T. Hudson, F.G. Serpa, J.D. Gillaspy, and E. Takacs. Phys. Rev. A, **62** 042501:1-13 (2000).
19. J.M. Laming, C.T. Chantler, J.D. Silver, D.D. Dietrich, E.C. Finch, P.H. Mokler, and S.D. Rosner. Nucl. Instrum. Methods Phys. Res. B, **31**, 21 (1988).
20. H.G. Berry and M. Hass. Ann. Rev. Nucl. Part. Sci. **32**, 1 (1984).
21. I. Martinson. Phys. Scr. **23**, 126 (1981).
22. C.J. Hailey, R.E. Stewart, G.A. Chandler, D.D. Dietrich, and R.J. Fortner. J. Phys. **B18**, 1443 (1985).
23. D.D. Dietrich, G.A. Chandler, R.J. Fortner, C.J. Hailey, and R.E. Stewart. Phys. Rev. Lett. **54**, 1008 (1985).
24. J.-P. Briand, M. Tavernier, P. Indelicato, R. Marrus, and H. Gould. Phys. Rev. Lett. **50**, 832 (1983).
25. H.F. Beyer, R.D. Deslattes, P. Indelicato, K.D. Finlayson, and D. Liesen. GSI Annual Report, 1989, p. 143; H.F. Beyer, P. Indelicato, K.D. Finlayson, D. Liesen, R.D. Deslattes, F. Folkmann, and R.E. La Villa. Phys. Rev. A, **43**, 223 (1991).
26. C.T. Chantler, J.M. Laming, D.D. Dietrich, W.A. Hallett, R. McDonald, and J.D. Silver. Phys. Rev. A, **76**, 042116-1-19 (2007).
27. J.D. Silver, A.F. McClelland, J.M. Laming, S.D. Rosner, G.C. Chandler, D.D. Dietrich, and P.O. Egan. Phys. Rev. A, **36**, 1515 (1987).
28. H.-D. Betz. Rev. Mod. Phys. **44**, 465 (1972).
29. K. Shima, T. Mikumo, and H. Tawara. At. Dat. Nucl. Dat. Tables, **34**, 357 (1986).
30. L.C. Northcliffe and R.F. Schilling. Nucl. Data Tables, **A7**, 233 (1970).
31. J.F. Ziegler. *In* The stopping and ranges of ions in matter. *Edited by* J.F. Ziegler. Pergamon, Oxford, UK. 1980.
32. U. Littmark and J.F. Ziegler. *In* The stopping and ranges of ions in matter. *Edited by* J.F. Ziegler. Pergamon, Oxford, UK. 1980.
33. A.F. McClelland, J.S. Brown, B.P. Duval, E.C. Finch, H.A. Klein, J. Laursen, D. Lecler, P.H. Mokler, and J.D. Silver. Nucl. Instrum. Methods Phys. Res. B, **9**, 706 (1985).
34. P. Beiersdorfer. Nucl. Instrum. Methods Phys. Res. B, **56/57**, 1144 (1991).
35. C.T. Chantler. Appl. Opt. **32**, 2371 (1993).
36. C.T. Chantler. Appl. Opt. **32**, 2398 (1993).
37. C.T. Chantler, J.D. Silver, and D.D. Dietrich. Appl. Opt. **32**, 2411 (1993).
38. C.T. Chantler. Ph.D. thesis. Oxford. 1990.
39. P.J. Mohr. At. Data Nucl. Data Tables, **29**, 453 (1983).
40. W.R. Johnson and G. Soff. At. Data Nucl. Data Tables, **33**, 405 (1985).
41. G.W. Erickson. J. Phys. Chem. Ref. Data, **6**, 831 (1977).
42. S. Klarsfeld and A. Maquet. Phys. Lett. **43B**, 201 (1973).
43. G.W.F. Drake. Can. J. Phys. **66**, 586 (1988).
44. L.A. Vainshtein and U.I. Safranova. Phys. Scr. **31**, 519 (1985).
45. J. Macek. Beam-foil spectroscopy. Vol. 2. *Edited by* I.A. Sellin and D.J. Pegg. Plenum Press, New York. 1975. p. 781.
46. J.M. Laming. Ph.D. thesis, Oxford. 1988.
47. C.T. Chantler and R.D. Deslattes. Rev. Sci. Instrum. **66**, 5123 (1995).
48. A. Chetioui, K. Wohrer, J.P. Rozet, A. Jolly, C. Stephan, D. Belkic, R. Gayet, and A. Salin. J. Phys. **B16**, 3993 (1983).

49. L.A. Vainshtein and U.I. Safranova. At. Data Nucl. Data Tables, **21**, 49 (1978).
50. L.A. Vainshtein and U.I. Safranova. At. Data Nucl. Data Tables, **25**, 311 (1980).
51. G.W.F. Drake. *In* The spectrum of atomic hydrogen: advances. *Edited by* G.W. Series. World Scientific, Singapore. 1988. pp. 137–241.
52. H.J. Hay and P.B. Treacy. Aust. J. Phys. **40**, 125 (1987).
53. A. Corney. Atomic and laser spectroscopy. Clarendon, Oxford, UK. 1986.
54. E.U. Condon and G.H. Shortley. The theory of atomic spectra. CUP, Cambridge, UK. 1987.
55. M.R.C. McDowell and J.P. Coleman. Introduction to the theory of ion-atom collisions. North-Holland, Amsterdam. 1970.
56. K. Omidvar. Phys. Rev. **153**, 121 (1967).
57. R.E. Olson, J. Ullrich, and H. Schmidt-Böcking. Phys. Rev. A, **39**, 5572 (1989.
58. B.L. Moisewitsch and S.G. Stockman. J. Phys. B, **13**, 2975 (1980).
59. R.Shakeshaft and L. Spruch. J. Phys. B, **11**, L457 (1978).
60. R. Shakeshaft. Phys. Rev. A, **20**, 779 (1979).
61. J.S Briggs and L. Dubé. J. Phys. B, **13**, 771 (1980).
62. W.J. Humphries and B.L. Moisewitsch. J. Phys. B, **B17**, 2655 (1984).
63. D.Z. Belkić, R. Gayet, and A. Salin. Comput. Phys. Commun. **32**, 385 (1984).
64. P.A. Amundsen and D.H. Jakubassa. J. Phys. B, **13**, L467 (1980).
65. J. Macek and S. Alston. Phys. Rev. A, **26**, 250 (1982).
66. L.J. Dubé. J. Phys. B, **17**, 641 (1984).
67. J. Eichler and F.T. Chan. Phys. Rev. A, **20**, 104 (1979).
68. L.J. Dubé and J. Eichler. J. Phys. B, **18**, 2467 (1985).
69. J. Eichler. Phys. Rev. A, **32**, 112 (1985).
70. J.M. Laming. Nucl. Instrum. Methods Phys. Res., Sect. B, **43**, 359 (1989).
71. D.Z. Belkić, R. Gayet, and A. Salin. Phys. Rep. **56**, 279 (1979).
72. R.K. Janev and H. Winter. Phys. Rep. **117**, 265 (1985).
73. H.A. Bethe and E.E. Salpeter. Quantum mechanics of one- and two-electron atoms. Springer-Verlag, Berlin, Germany. 1957; Plenum, New York. 1977.
74. K. Omidvar. At. Data Nucl. Data Tables, **28**, 1 (1983).
75. K. Omidvar. At. Data Nucl. Data Tables, **28**, 215 (1983).
76. R. Anholt, W.E. Meyerhof, C. Stoller, E. Morenzoni, S.A. Andriamonje, J.D. Molitoris, O.K. Baker, D.H.H. Hoffmann, H. Bowman, J.S. Xu, Z.Z. Xu, K. Frankel, D. Murphy, K. Crowe, J.O. Rasmussen. Phys. Rev. A, **30**, 2234 (1984).
77. R. Anholt. Phys. Rev. A, **31**, 3579 (1985).
78. W.E. Meyerhof, R. Anholt, and X.Y. Xu. Phys. Rev. A, **35**, 1055 (1987).
79. R. Anholt, W.E. Meyerhof, H. Gould, C. Munger, J. Alonso, P. Thieberger, and H.E. Wegner. Phys. Rev. A, **32**, 3302 (1985).
80. R. Anholt and W.E. Meyerhof. Phys. Rev. A, **33**, 1556 (1986).
81. R. Anholt, C. Stoller, J.D. Molitoris, D.W. Spooner, E. Morenzoni, S.A. Andriamonje, W.E. Meyerhof, H. Bowman, J.S. Xu, Z.Z. Xu, J.O. Rasmussen, and D.H.H. Hoffmann. Phys. Rev. A, **33**, 2270 (1986).
82. J.P. Rozet, A. Chetioui, P. Bouisset, D. Vernhet, K. Wohrer, A. Touati, C. Stephan, and J.P. Grandin. Phys. Rev. Lett. **58**, 337 (1987).
83. W.A. Hallett. Ph.D. thesis, Oxford. 1991.
84. A.F. McClelland. Ph.D. thesis, Oxford. 1989.